Acta Materialia 318 (2026) 122638

Contents lists available at ScienceDirect

Acta Materialia

journal homepage: www.elsevier.com/locate/actamat

Full length article

Field inhomogeneous distributions and local percolations in Ag-$BaTiO_3$ ceramic-metal composites: The role of microstructural variability

Ina Turcan [a,b], Leontin Padurariu [a], Vlad Alexandru Lukacs [a,*], Radu Stefan Stirbu [a], Cristina Elena Ciomaga [c], Roxana Elena Patru [d], Fereshteh Falah Chamasemani [e], Roland Brunner [e], George Stoian [f], Liliana Mitoseriu [a,*], Donatella Giuranno [g,*]

[a] Dielectrics, Ferroelectrics & Multiferroics Group, Faculty of Physics, Alexandru Ioan Cuza University of Iasi, 11 Carol I Blvd., 700506, Iasi, Romania
[b] "Ion Ionescu de la Brad" Iasi University of Life Sciences, 3 Mihail Sadoveanu Alley, 700490, Iasi, Romania
[c] Department of Exact & Natural Sciences, Institute of Interdisciplinary Research, Alexandru Ioan Cuza University of Iasi, 11 Carol I Blvd., 700506, Iasi, Romania
[d] National Institute for Materials Physics, Atomistilor 405A, Magurele, 077125, Romania
[e] Department Microelectronics, Materials Center Leoben Forschung GmbH, 12 Vordernberger Str, 8700, Leoben, Austria
[f] National Institute of Research and Development for Technical Physics, Iasi, 700050, Romania
[g] Institute of Condensed Matter Chemistry & Technologies for Energy, National Research Council of Italy, Via De Marini 6, 16149, Genoa, Italy

ARTICLE INFO

Keywords:
$BaTiO_3$
Ceramic-metal composite
Percolation
Dielectric properties
3D tomography

ABSTRACT

This work investigates how composition and microstructural variability influence the dielectric properties of xAg–(1–x)$BaTiO_3$ ceramic-metal composites (denoted as CerMet) through combined modelling/experimental approach. Virtually generated microstructures predict different percolation ranges depending on microstructural modifications. To check such effect, a range of compositions with $x \leq 20$ vol.% were synthesized using single-step or two-steps sintering to ensure compositional integrity and similar $BaTiO_3$ grain size. During the consolidation, Ag undergoes melting, migration, and infiltration, generating intricate metal–ceramic connectivity. The permittivity exhibits percolation-like increases near critical compositions around 5, 11.5, and >20 vol.%, reaching a maximum value of $\varepsilon_r \approx 17{,}000$ at 20 °C with tan $\delta \leq 2\%$ (at 10 kHz) for $x = 11.5$ vol.%. The high permittivity compositions selected for X-Ray tomography and detailed microscopic analyses revealed 3D microstructures with specific features, where field concentration ("hot spots") occurs. These results demonstrate how metal melting during sintering governs microstructural evolution and variability and the important role of the elongated and tortuous filler structures in increasing the CerMet effective permittivity towards giant values towards the percolation limits.

1. Introduction

The integration of dissimilar materials with divergent physico-chemical properties in composite structures offer a large research room for generating interesting and new properties. Through the careful selection of materials and the accurate tuning of their composition and microstructures, their functional properties can be elevated to a level that surpasses the state-of-the art characteristics of single-phase materials. Among the wide class of bulk composites, ceramic-metal composites (denoted as CerMets) consist of a ceramic matrix filled with metallic particles and combine the high temperature resistance, hardness and insulating character specific to the ceramic component with the plastic deformation and electrical and thermal conductivity of metals [1–3]. From an electrical point of view, the presence of metallic fillers provides a larger permittivity, which was intuitively explained as being the result of the formation of nano/micro-capacitors inside the dielectric matrices [2]. Calculations realized by Finite Element Methods (FEM) solving locally the electrostatic equations with boundary conditions, demonstrated that permittivity increase is related to the electrostatic energy intensification created by the concentration of high field in the dielectric regions in between the metallic particles (so called "hot-spots") [4,5]. Increases in filling factor result in a permittivity increase, approaching significantly high levels. These "giant" values are located below the percolation limit, which is characterised by a critical composition value, denoted as the percolation threshold f_c [6,7 *and refs herein*]. The electrical properties around the percolation threshold

* Corresponding authors.
E-mail addresses: vlad.lukacs@uaic.ro (V.A. Lukacs), lmtsr@uaic.ro (L. Mitoseriu), donatella.giuranno@ge.icmate.cnr.it (D. Giuranno).

https://doi.org/10.1016/j.actamat.2026.122638
Received 11 March 2026; Received in revised form 9 July 2026; Accepted 7 August 2026
Available online 8 August 2026
1359-6454/© 2026 The Authors. Published by Elsevier Inc. on behalf of Acta Materialia Inc. This is an open access article under the CC BY-NC-ND license (http://creativecommons.org/licenses/by-nc-nd/4.0/).

f_c show dramatic changes and non-linear behaviour as a function of composition (filling factor f), described by universal scaling laws [6]:

$$Property \sim |f - f_c|^{\pm q}, \quad (1)$$

where q is a critical exponent which can assume different values, depending only on the spatial dimension of the composites. The percolation threshold f_c is not an universal constant, but it is strongly dependent on the composite's microstructure, *i.e.* on the size and shape of the filler inclusions, shape factor, size distribution, or clustering. Above the percolation limit, the metal particles come into contact, thus forming a large conductive cluster, and the overall material turns into a conductive one [7]. As a result of the identical mechanism of field concentration, the use of ferroelectric ceramic as matrices influences the non-linear dielectric characteristic (tunability) as well as the ferro/piezoelectric responses. In certain concentrations, these responses may exceed those specific to the ferroelectric matrices [8].

From an experimental perspective, the fabrication of di-phase CerMet composites poses several challenges, predominantly related to the elevated temperatures necessary for the ceramic processing [1–3]. At such high temperatures, which are indispensable for optimal ceramic densification, reciprocal ion interdiffusion may take place at the interphases that delineate dissimilar materials. This phenomenon is accompanied by the possible formation of secondary phases. In order to achieve pure di-phase CerMet composites, it is essential to select materials that are chemically inert and possess reduced reciprocal solubility. In addition, it is necessary to implement careful thermal strategies for consolidation. The use of noble metals or their alloys as fillers was preferred in CerMet composites, because of their excellent electrical conductivity and for limiting the interphase chemical reactivity during the sintering step.

In recent years, a significant number of studies have been dedicated to the electrical properties of various material combinations in CerMets. Among these, Ag-$BaTiO_3$ (Ag-BT) family represents one of the most investigated material combinations [9–14], because of Ag's exceptional electrical conductivity and its extremely low solubility into the BT matrix. This property is widely acknowledged in literature, as discussed in a previous paper [5], and is backed by thorough careful research [9,10]. However, the sintering temperature range of BT ceramics (1100–1250 °C) encompasses the melting temperature of Ag (960 °C). During the ceramic sintering (closure of open porosity and grain growth), Ag melts and move through the open pores. Although silver demonstrates low wettability on the BT interfaces, the molten metallic phase experiences substantial volume expansion due to the absorption of a considerable amount of oxygen from the environment (approximately up to 20 times) [15–17]. This phenomenon serves as a driving mechanism for the migration of Ag over extended distances through the open ceramic pores, resulting in the creation of an interconnected network of uneven inclusions within the final composites. The melting and infiltration of liquid Ag in between the percolated ceramic pores may also produce silver depletion through the open pores towards the composite surface. Furthermore, these processes may generate microstructural differences, *i.e.* various metallic filler shapes, which will result in different functional properties. Because of these effects, the Ag-BT CerMet system is highly intriguing to investigate in depth, both in terms of the microstructural evolution and concerning its effect on the effective electrical properties. The literature findings on the permittivity increase in Ag-BT composites in relation to the Ag filling factor are quite contradictory, and in addition, they do not match the expected values predicted by the percolation theory or by effective field calculations [8–13]. In some studies, when the filling factor is low, the increase in permittivity occurs much quicker than expected [5,11,13]. In other research, adding a small amount of metal causes the permittivity to decrease, but later it goes back up to high values [10,12]. Some reports show that permittivity starts to rise, but then drops again when the filling factor is high [11,18]. Such a wide range of dielectric results could be attributed to several factors: (i) the impact of density, which was inconsistent in different sample series (and seldom documented, in fact), (ii) the fluctuations of nominal compositions caused by Ag depletion at free surfaces; and (iii) microstructural influences (*e.g.* the connectivity scheme and the size, shape, and distribution of fillers varied across all compositions in a CerMet sample series). Apart from a limited number of reports [8], the literature predominantly examined the impact of composition in Ag-BT CerMets. Considering the diverse trends in the permittivity as a function of filler concentration [8–18], we considered that investigating the influence of the resulting microstructures on the percolation limit and the electrical characteristics of these composites deserves a thorough experimental-modeling analysis.

The paper is organized as follows: Section 2 presents the preliminary finite element (FEM) simulations performed on various types of model microstructures in order to find specific ones characterised by high permittivity values, nearby the percolation ranges, as a basis for the experimental part of this study. Section 3 details the methodology and experimental design for the sample preparation of xAg-(1-x)BT composites and their thorough characterisation. Section 4 presents the dielectric results gathered at various temperatures and frequencies as a function of Ag filling factor and discuss in detail the role of metallic addition on the dielectric constant and losses, ac-conductivity, frequency dispersions and on the microstructural assigned R, C circuit components (BT bulk, ceramic grain boundaries and Ag-BT interfaces) derived from Impedance Spectroscopy analyses. Further, a set of compositions showing enhanced permittivity have been selected for a detailed three-dimensional microstructural investigation providing 3D microstructures with two levels of resolution, which have been further used to compute numerically the local field distributions. This part of the study was aimed to decipher the specific microstructural details related to the obtained highest permittivity values. Finally, the last section presents the implications of these findings and concludes the study.

2. Model

The critical filling factor (percolation limit) depends on the filler shape, size and distribution, or clustering degree. Its value was predicted in the range of 15 vol.% to 30 vol.% for equiaxed conductive particles embedded into a dielectric matrix (about 30 vol.% for conductive spherical inclusions randomly dispersed into an insulator continuous medium), and is strongly reduced for elongated filler structures [6,7,19–21]. A much broader experimental range of values for the *percolation threshold* f_c has been reported as result of inhomogeneous filler distribution, aggregation, to presence of secondary phases or porosity effects [6,7,19–23 *and refs. herein*].

To examine the effect of CerMet microstructures on the percolation threshold, several types of phase configurations have been suggested by examining standard Ag inclusions produced in Ag-BT metal-ceramics in earlier studies [6,8]. The first arrangement, referred to as *Configuration 1* (Fig. 1, (a)), pertains to the scenario where the Ag component fully melted during the sintering process, leading to metal inclusions filling the available space between the grains after solidification. This type of configuration was numerically developed by generating spherical grains with random positions until their filling factor (density) reaches a desired value. The spherical grains were allowed to overlap (in order to describe the formation of the necks between grains), and conductive properties were assigned to the free regions in between the grains. The second case, denoted as *Configuration 2* (Fig. 1, (b)), corresponds to the situation of randomly intermixed phases. The algorithm for generating such structures with desired amounts of the conductive components and the calculations of the effective permittivity was described in a former paper [24]. The third case, which is described by *Configuration 3* (Fig. 1, (c)), corresponds to the spherical conductive inclusions embedded into the dielectric matrix. The procedure for generating such microstructures is very similar, but complementary to the method of producing the *Configuration 1* (Fig. 1, (c)), *i.e.* the spherical conductive inclusions are

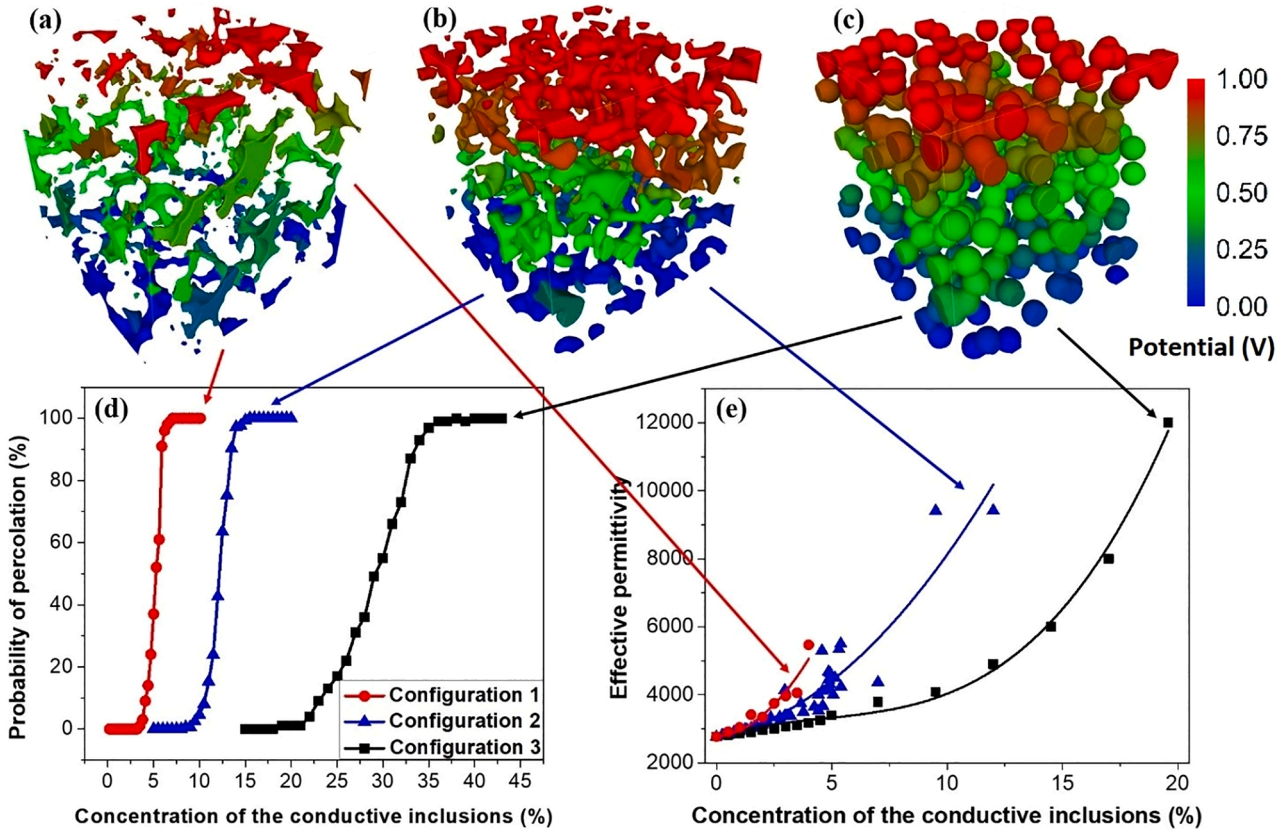


Fig. 1. Example of three types of Ag microstructures inside the BT continuous matrix (not represented) considered in the Finite Element Method - based simulations: *Configuration 1* (a), *Configuration 2* (b), and *Configuration 3* (c). The probability of percolation for various concentrations of the conductive phase (d); and the effective permittivity *vs.* the conductive phase filling factor (e). The color scale in (a, b, c) indicates the local electric potential values on the Ag phase with parallel plate capacitor boundary conditions (the capacitor was subjected to a voltage of 1 V).

generated in random positions until a desired concentration is reached. Initially, tens of thousands of these virtual microstructures (across all three configurations) were created at different concentrations of the conductive filler to reveal the direct conductive paths linking the capacitor system's bottom and top electrodes (*i.e.*, the percolation process). The likelihood of percolation in relation to the filling factor (Fig. 1, (d)) was assessed by tallying the number of percolated systems out of 100 created ones at the identical concentration. After determining the local field in each element by using the electrostatic boundary conditions (plan parallel capacitor with Ag-BT composite inside, subjected to a voltage of 1 V), the total electrostatic energy of the system was computed by summing all the local contributions per elements:

$$W_{tot} = \frac{1}{2}\sum \varepsilon_{loc} E_{loc}^2 \tag{2}$$

and then, the effective permittivity ε_{eff} was determined on the basis of eq. $W_{tot} = W_{eff}$, where W_{eff} is given by:

$$W_{eff} = \frac{1}{2}\varepsilon_{eff} E_{appl}^2, \tag{3}$$

where E_{appl} is the external applied electric field. The results of such calculations are summarized in Fig. 1, for the numerical values of local permittivity: 2700 for BT and 10^8 for Ag.

The microstructures corresponding to the three types of Ag configurations inside the ceramic matrix are shown in Fig. 1, (a-c) and the derived percolation probability and the computed effective permittivity *vs.* the metal concentration in Fig. 1, (d) and Fig. 1, (e), respectively. The graphs presented in Fig. 1, (d) indicate that the three configurations display completely different values for the critical percolation filling factor. For a better view of the microstructures, in the *Annex* are also shown the representations of successions of 2D slices into the 3D microstructures. The sections are realized parallel to the planar electrodes (see *Annex – Supplementary Material, Fig. S1 & configuration 1.mp4, configuration 2.mp4, configuration 3.mp4)* and the different colours indicate: the ferroelectric ceramic component (grey), isolated conductive inclusions (green), conductive inclusions connected to the bottom electrode (blue), conductive inclusions connected to the top electrode (orange) and conductive percolated channels between the two electrodes (brown).

The minimum critical percolation concentration of about 5 vol.% was found in *Configuration 1*, as the conductive particles are somewhat more elongated compared to the other configurations, leading to a greater likelihood of connecting/touching each other and achieving the overall conductive state, even with reduced metallic quantities. The critical percolation threshold rises to approximately 12 vol.% for *Configuration 2* and attains a maximum of 25–30 vol.% for *Configuration 3*, nearing the anticipated reported values for isolated spherical inclusions into a continuum dielectric [19–21]. For a few selected microstructures belonging to each one of the three configurations and filling factors below 4 vol.% for Configuration 1, below 12 vol.% for Configuration 2, and below 20 vol.% for Configuration 3, *i.e.* below their corresponding percolation limit, the effective permittivity was computed by FEM calculations and is shown in Fig. 1, (e).

The three types of microstructures exhibit different permittivity values at a given concentration in the dielectric region below the lowest percolation limit; the composite samples with *Configuration 1* - like microstructures exhibit the highest permittivity values and the fastest permittivity increase *vs.* the filler concentration. Consequently, this configuration offers a very good way to achieve a strong increase in the

dielectric constant when a relatively low concentration of the conductive phase (below 4 vol.%) is required. Its corresponding permittivity maximum is limited to values of about 5000–6000, with respect to the value of the dielectric ceramic matrix of 2700. As the concentration of the conductive phase rises to around 12 vol.%, *Configuration 2* offers the most promising way to achieve greater permittivity values (around 10,000). For the microstructures that correspond to *Configuration 3*, the effective permittivity can also be increased to bigger values of ≈12,000 for higher concentrations of the conductive phase, over 20 vol.%.

Therefore, by embedding metallic inclusions with different geometries and local percolated regions, higher permittivity values can be reached for compositions close to different critical metallic filling factors. This finding is significant and may be particularly appealing for applications, provided that the associated dielectric losses remain low [22]. The field is zero inside the conductor component and almost zero inside the dielectric regions contained inside the metallic clusters, but it becomes substantially inhomogeneous inside the dielectric volume, due to the electric boundary conditions. As a result, distinct dielectric regions experience electric fields that may differ to a large extent from the applied external one. Although permittivity strongly increases as a result of field intensification in dielectric regions, the breakdown field may be overcome and the composite sample may not be able to withstand higher fields in order to attain large energy storage capacity [25]. The dielectric, ferroelectric, and piezoelectric responses are also impacted by the microstructural variations since the local field distribution is dependent on the filler geometry (size, distribution, and connection) in addition to the filler composition. It is important to emphasize that different microstructure types with distinct geometrical properties can offer different ranges for the permittivity increase and percolation limits. Consequently, a set of Ag-BT metal-ceramic composites have been processed and studied in order to examine the possibility of adjusting the dielectric properties by composition, while also producing different types of microstructures, taking into account the significant role of the metal microstructures inside the ceramic matrix. Keeping in mind that permittivity of $BaTiO_3$ ceramics is influenced by grain size [26,27], the sintering procedure was optimized to achieve similar and uniform grain sizes in the BT ceramic component, while preserving the nominal compositions of Ag (without Ag depletion) across the whole compositional range.

3. Sample preparation and experimental details

A set of xAg-(1-x)$BaTiO_3$ (Ag-BT) CerMet composites with x = 0, 1, 2, 3, 4, 5, 6, 8, 10, 11.5, 12, 13.5, 15, 17.5 and 20 (vol.%) have been prepared by simple wet mixing of commercial silver microparticles (Sigma Aldrich, purity ≥99.9% and ≈4 μm particle size, Fig. 2(a)) and $BaTiO_3$ (BT) fine nanopowders (Sigma Aldrich, purity ≥99%, ≈60 nm particle size, Fig. 2(b)), similarly as described in ref [5]. The samples with Ag additions x ≤ 12 vol.% have been all sintered in a single step (SSS) at 1200 °C for 2 h [5], which was established by testing as an optimum for a good densification and for preserving the Ag composition. However, when using the same sintering strategy for larger Ag additions (x > 12 vol.%), Ag depletion towards the external CerMet surfaces was noticed. Therefore, for the compositions in the range of 12 < x ≤ 20 (vol.%), a two-steps sintering (TSS) strategy was used, with a long intermediate sintering stage at a lower temperature of 930 °C for 12 h was introduced, followed by a short sintering step at 1200 °C for 10 min, in order to prevent the Ag loss and preserve the nominal compositions while obtaining similar BT grain sizes (Fig. 2). The intermediate long sintering step at a temperature below the melting point of Ag was intended to allow the partial densification of the ceramic matrix for closing the pores of BT, in order to avoid the Ag depletion by liquid phase migration through the percolated porosity. This method is denoted as two-steps sintering (TSS) in the following. However, it was expected that the use of such a reduced sintering temperature, even for a longer time of 12 h, may generate a lower sample density. Indeed, the resulting relative densities shown in Fig. 2(c), as determined by Archimedes' method (using the theoretical density of Ag: 10.49 g/cm^3 and of $BaTiO_3$: 6.02 g/cm^3) take values between 88% and 95% (see *Table SI, Annex – Supplementary Material*) for the compositions x ≤ 12 vol.% sintered by SSS method and have lower values for higher metallic additions: 12< x ≤ 20 (vol.%) sintered by TSS, being in the range of (82 ÷ 83.5)%. Other attempts to better densify these compositions at higher sintering temperature or for a longer time produce a grain size increase

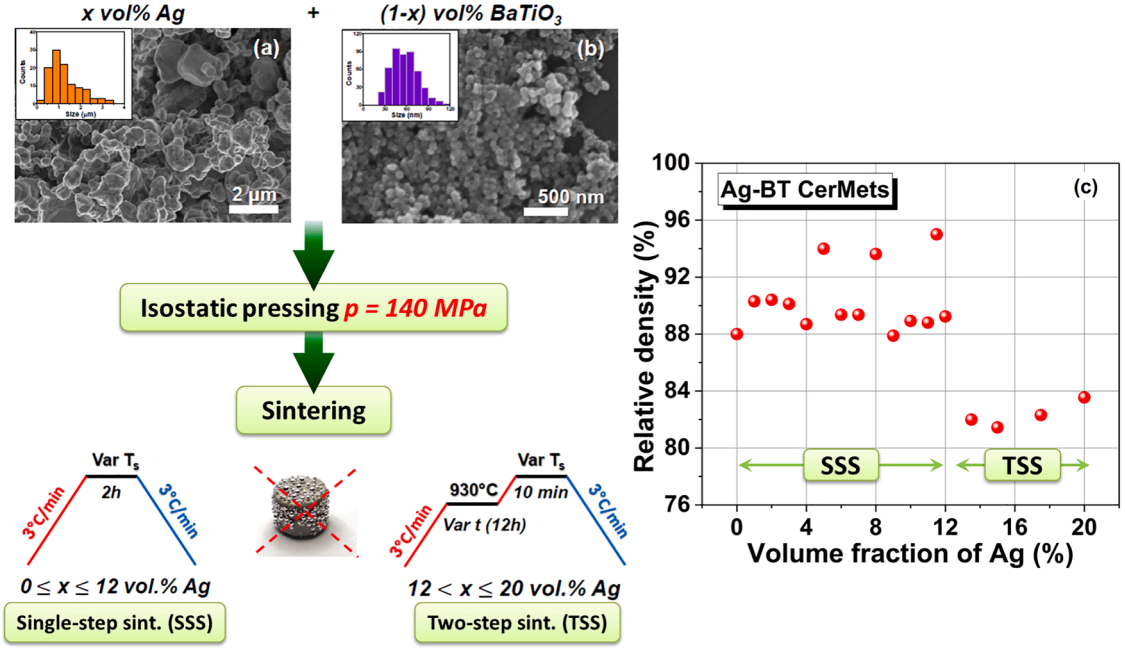


Fig. 2. Diagram presenting the processing procedure for producing Ag-BT CerMets with different compositions, sintered by single step-sintering (SSS) for x ≤ 12 vol.% and by two-steps sintering (TSS) method, which also shows the microstructures of the initial Ag particles (a) and BT nanopowders (b); the final CerMet composites' relative density *vs.* Ag filling factor (c).

of the BT ceramics, besides the loss of some Ag amounts. To preserve the average grain size of the final ceramic component and nominal compositions, the sintering technique was left unchanged, thus being aware on the porosity effects for the Ag addition in the range above 12 vol.% Ag additions.

The crystalline phases have been identified with a SHIMADZU XRD 6000 diffractometer using Ni-filtered CuKα radiation (λ = 1.5418 Å), with a scan step of 0.02° and a counting time of 1 s/step, for 2θ ranging between 20° and 80°. The crystalline structure was determined by Rietveld refinement carried out using the General Structure Analysis System (GSAS) software package [28]. The morphology of the starting powders and of the CerMet composites was observed by using high resolution scanning electronic microscopy (Crossbeam System Neon 40ESB FIB-SEM from Carl Zeiss) coupled with Energy-dispersive X-ray spectroscopy (EDS). The grain size distributions of the BT component were determined by counting over ≈350 individual grain measurements, through the use of ImageJ image analyser software on the collected SEM micrographs.

For a better inspection of the volume distribution of Ag filler inside the samples, 3D micro X-ray computed tomography (μ-XCT) was employed to provide the 3D distribution in a few selected compositions (x = 5, 11.5 and 20 vol.%), by using a nanotom from General Electrics (GE) [29,30]. The voxel size was 0.67 μm and the size of the selected volume of interest (VOI) for the analysis was: 615 × 520.6 × 45.6 μm^3. Python libraries (including Numpy, Scipy, Scikit-image, Matplotlib, and Scikit-fmm) and Avizo® were used to carry out μ-XCT data processing and visualization.

Additionally, a focused ion beam (FIB) of Ga ions accelerated at 30 kV has been employed perpendicular to the sample surface, generating a cross-section to reveal local particularities concerning the shape and sizes of the metallic fillers, as well as for observing local percolated regions, whose micron-scale details remain visible. The ion beam can precisely remove material through sputtering or milling, and the SEM allows for high-resolution imaging of the modified area. Volumes of 20 × 20 × 20 μm^3 have been extracted to prepare 3D reconstructions of CerMet samples by recording 2D slices with approx. 10 nm/pixel in the XY plane and slice spacing of around 15 nm (z_{depth}).

The electrical measurements were performed in a parallel plate capacitor configuration, after applying Ag paste electrodes onto the clean polished surfaces of disk-shaped ceramic samples. The dielectric measurements were realised by using an Agilent E4980 A Precision LCR Meter impedance bridge for temperatures between room temperature and 140 °C and 180 °C in the frequency range from 20 Hz up to 2 MHz.

4. Results and discussions

4.1. Phase and microstructural characterisation

After sintering, di-phase CerMet composites containing only the parent phases: *Fm3m* cubic Ag (PDF nr. 01–087–0718) with unit cell parameters: a = b = c = 4092 Å) and perovskite BT, with compositions close to the expected nominal ones have been obtained *(Fig. S2, Annex – Supplementary Material)*. The perovskite BT matrix presents a superposition of orthorhombic (O) and tetragonal (T) polymorphs, with a weight of around 50%, for all the compositions. For example, the composition x = 5 vol.% (corresponding to ≈8 wt.% Ag) presents a relative weight O/T of 44/48, with unit cell parameters for (O): a = 3.9997 Å; b = 5.6942 Å; c = 5.7137 Å and for (T) symmetry: a = b = 3.9992 Å; c = 4.0413 Å and tetragonality c/a = 1.0105 [5]. No notable shifts of the BT peaks are noticed in the composites, with respect to the pure BT patterns. This indicate that Ag incorporation into the BT is unlikely, in agreement with the literature data reporting a very limited solubility of Ag in the BT perovskite matrix [5,9,10,31].

For all compositions, including those with higher Ag content sintered in two steps, the SEM micrographs obtained on the fresh ceramic fractures (Fig. 3) reveal the presence of homogeneous ceramic grains with very similar Gauss-like grain size distributions in the ceramic BT matrix, with a clearly defined sharp maximum around 0.5–0.7 μm. Unlike the majority of CerMet samples, a quite broad distribution with a large number of grains in the range of 0.5–2 μm is observed for x = 5 vol.% Ag addition.

For all the compositions, the distribution of metal inclusions inside the ceramic matrix as determined by the SEM-BSE analyses looks quite inhomogeneous within the analysed volume, as shown in Fig. 4. The inclusions present variable sizes and shapes: fine equiaxed inclusions or elongated filaments coexist with large aggregated inclusions (either elongated or rounded in shape) and with bulky regions with sizes of about 20–30 μm diameters. It is important to note that both fine and bulky metallic inclusions, up to roughly ten times the normal BT ceramic grain size, can be detected at any filling factor value. The Ag inclusions

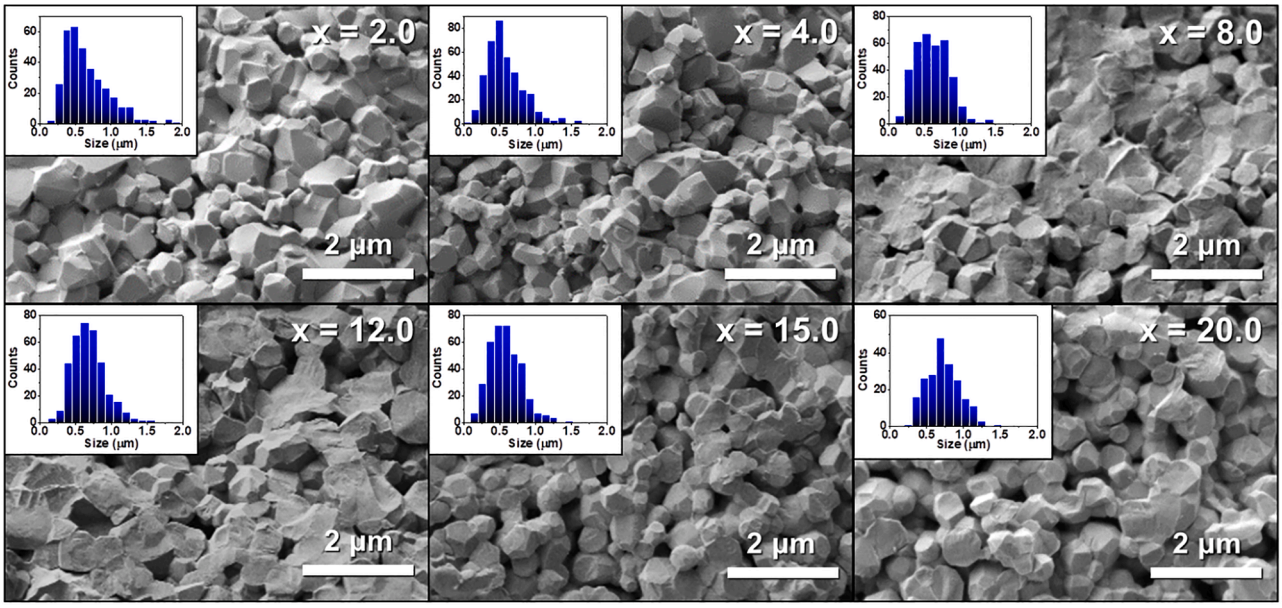


Fig. 3. SEM micrographs realized on fresh fracture of selected xAg-(1-x)$BaTiO_3$ CerMets (*Inset*: grain size distributions of the BT matrix) having the compositions: x = 2, 4, 8, 12, 15 and 20 vol.%.

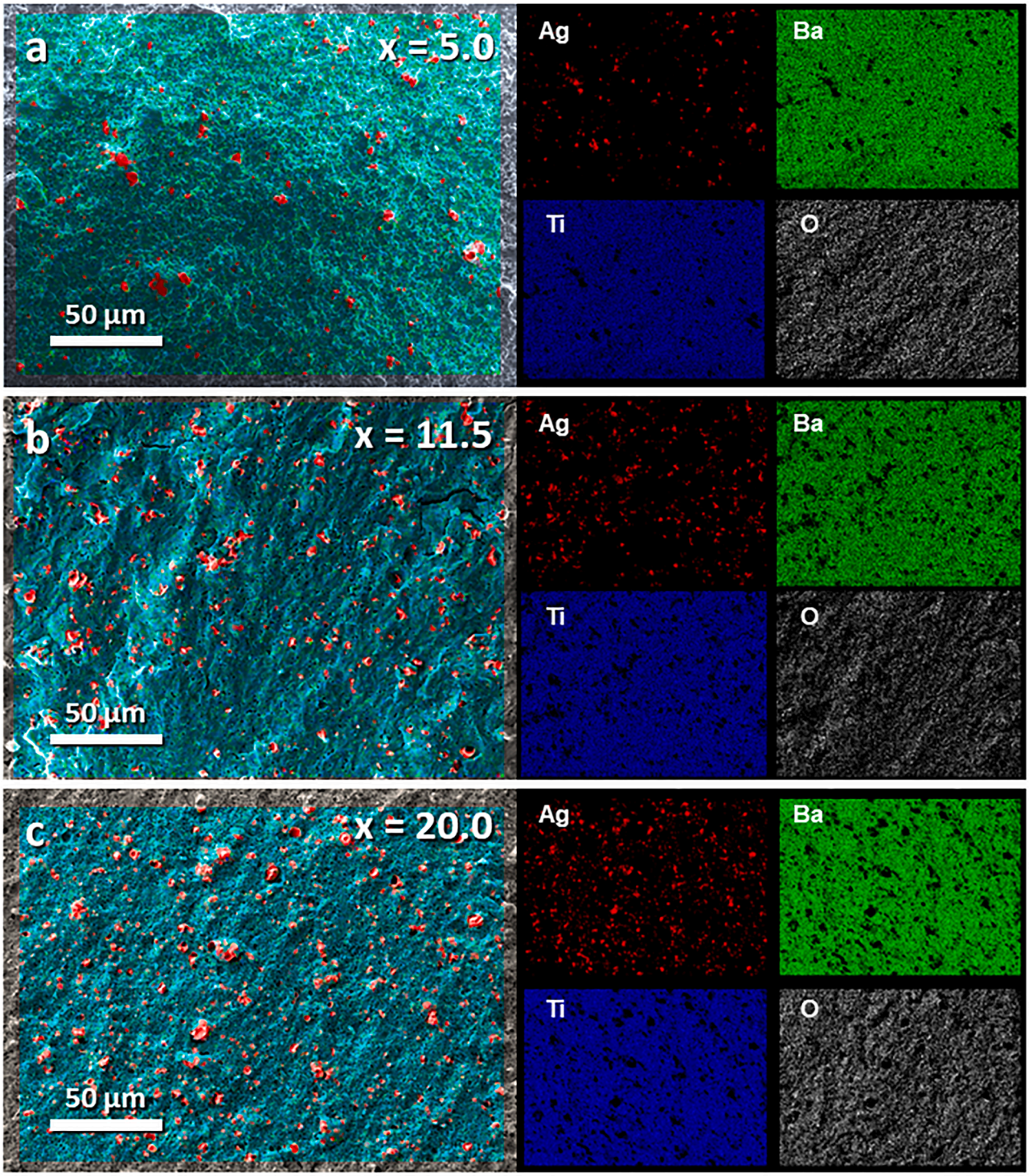


Fig. 4. Fresh fracture SEM micrographs with elemental mapping, indicating the distributions of Ag, Ba, Ti and O ions in the xAg-(1-x)$BaTiO_3$ CerMets, with the selected compositions x of: (a) 5 vol.%, (b) 11.5 vol.%, and (c) 20 vol.%.

generally seem to be slightly larger and better isolated at x = 20 vol.% (Fig. 4, c), and much more clustered at the composition x = 11.5 vol.% (Fig. 4, b). The melting of Ag inclusions during the consolidation process and their extensive migration through the percolated ceramic pores - which had not yet been sealed by sintering - allow the formation of large Ag structures at cooling. They can move within the available space and join with comparable amounts of melted Ag from other percolated porosity regions. Conversely, the fine ones are most probably produced in closed pores inside the ceramic body. The fine observed equiaxed Ag fillers can also be 2D sections of thin elongated Ag areas (filaments).

4.2. *Dielectric properties*

The real part of permittivity *vs.* temperature at variable frequencies are shown for all the compositions in Figs. *S3, Annex* and, for a fixed frequency of 10 kHz in Fig. 5 (a-c) for a direct comparison. Further, the temperature dependence of the corresponding dielectric loss *tanδ* are displayed in Figs. *S4, Annex* and the comparison (at f = 10 kHz) in Fig. 5

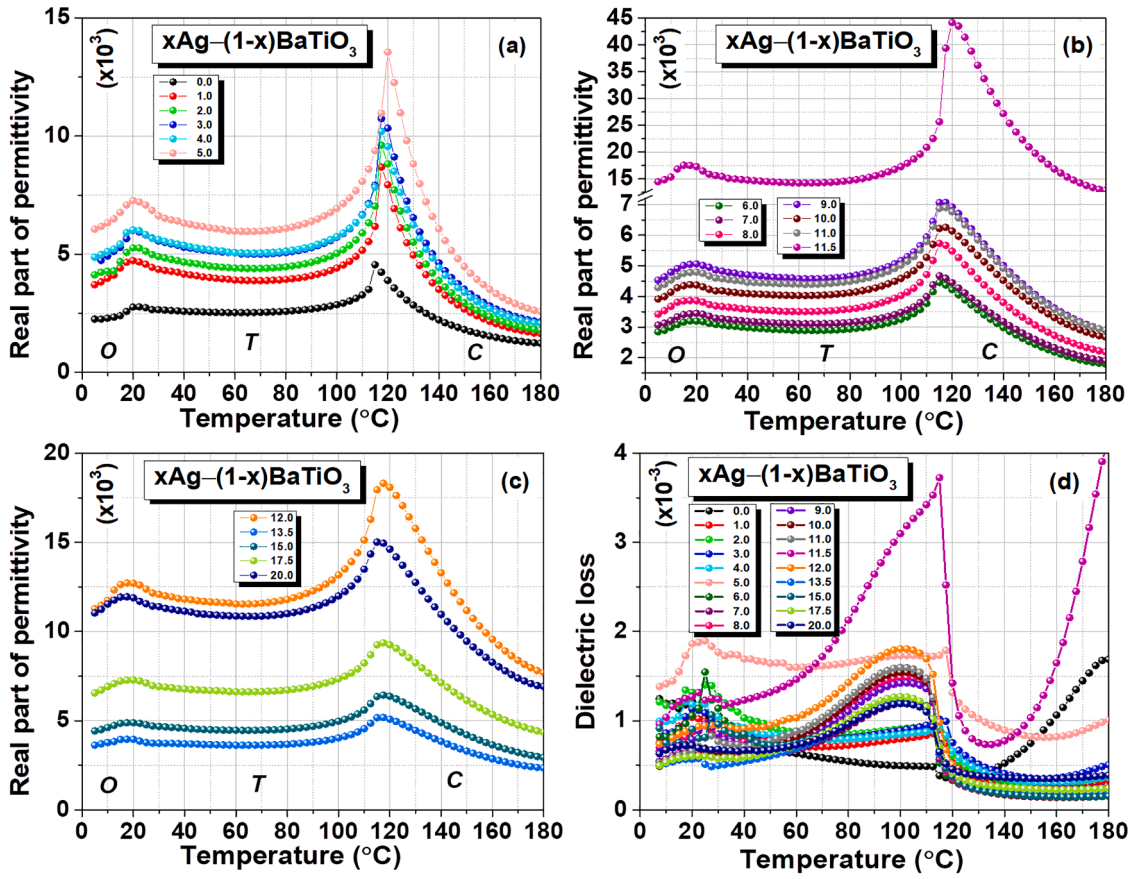


Fig. 5. Temperature dependence of the real part of permittivity (a, b, c) and of the dielectric loss *tanδ* (d) at the frequency of 10 kHz, for the xAg-(1-x)$BaTiO_3$ compositions (x in vol.%).

(d). Regardless of composition and frequency, it is noticed that all of the samples exhibit a similar trend above room temperature, which is derived from the typical dielectric behaviour characteristic to $BaTiO_3$ ferroelectric ceramics [32]. The permittivity and loss data show two distinct anomalies as a function of temperature. They originated from the polymorph transformations of the BT matrix: orthorhombic-to-tetragonal (O-T) in the range of 17–20 °C in the composites, with respect to about 22.5 °C for BT, and tetragonal-to-cubic (T-C) in the range of (120–121.5) °C for the composites, with respect to about 115 °C in the reference BT ceramic. Consequently, room temperature falls within the of O-T polymorph superposition range of all the compounds, thus supporting the findings of the XRD investigations concerning the orthorhombic-tetragonal superposition [5]. The critical temperatures for a particular composition are essentially insensitive to frequency, with fluctuations occurring within 1 °C in the 1 Hz - 1 MHz range. Overall, it is observed that the ferroelectric-paraelectric transition changes from a sharp one to a broader, diffuse one, when Ag filler is added. The inserting of metallic particles into the BT matrix alters the dielectric response by introducing competing forces due to the formation of internal Schottky barriers, screening, strain and defects at the metal-ceramic interfaces, which give rise to extrinsic contributions to the effective complex permittivity. The presence of metals inside the dielectric matrix may also change the ferroelectric domain structure and their mobility due to the modifications of mechanical and electrical local boundary conditions [33], thus resulting in a modulation of BT ceramic intrinsic ferroelectricity. Both intrinsic and extrinsic modifications interfere with the pure BT ferroelectric response and lead to modifications of the effective Curie constant and of its critical temperatures and to the broadening of the dielectric peak in the Curie range [34]. Nevertheless, the dielectric response remains dominated by the ferroelectric matrix at any composition, being thus described by a Curie-Weiss dependence, with renormalized constants.

The dependences of *tanδ vs.* temperature at selected frequencies (Figs. *S4, Annex*) show three regions with distinct loss increase or local maxima: (i) all the compositions present higher losses, particularly enhanced at low frequencies, with maxima at the structural transformation O-T; the stronger effect is observed for the compositions x = 6, 8, 9, 10, 11 and 15 vol.%; (ii) at the ferroelectric-paraelectric phase transformation (T-C), an anomaly of *tanδ* is also present, with higher losses in the ferroelectric phase, followed by an abrupt loss decay in the paraelectric state; this anomaly is not enhanced at low frequencies; and (iii) an increase of low frequency losses at high temperatures above the Curie range, as a typically thermally activated phenomenon which is boosted when temperature increases. The frequency dependences of the real and imaginary parts of permittivity presented in Figs. *S5* and *S6, Annex*, respectively, also confirm the presence of a low frequency dispersion, which is enhanced at the O-T transition and are prominent above the Curie range, and a relaxation in the range of (10^3–10^5) Hz activated in the ferroelectric state when approaching the Curie temperature (visible at 100 °C in Figs. *S5* and *S6*) and disappears in the paraelectric state. In addition to the field increase effect associated with the microstructures, as previously demonstrated by simulations in §2, such behaviour suggests the presence of complex dielectric relaxations that impact the permittivity values and specifically the losses.

A few observations are derived by observing the conductivity *vs.* frequency dependences shown in Fig. 6, a for all the compositions at room temperature and in detail, in Figs. *S7 (a-r)* from the *Annex: §4* at a few selected temperatures of: 10 °C, 50 °C, 100 °C, 150 °C and 180 °C). For all the samples, the ac conductivity σ_{ac} *vs.* frequency presents a similar growing trend when frequency increases, from values of about

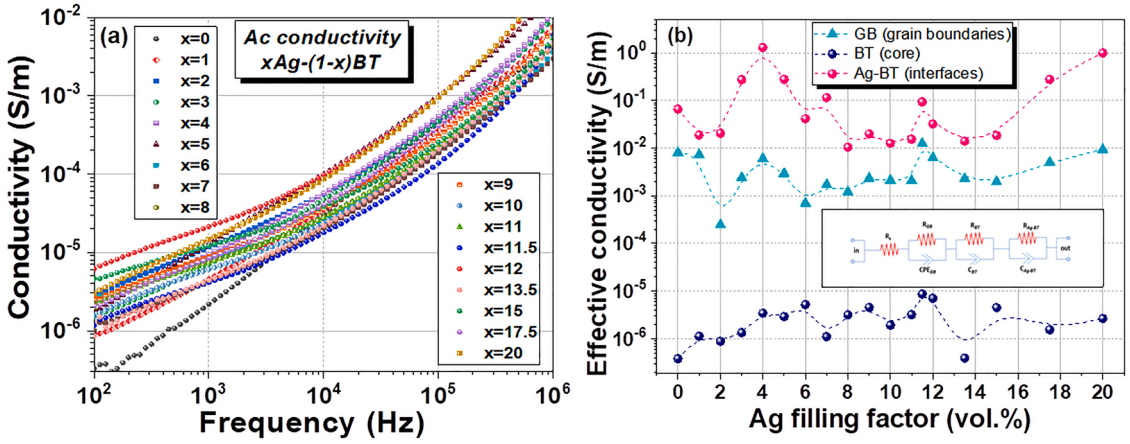


Fig. 6. (a) Frequency dependence of ac-conductivity (T = 20 °C) for the xAg-(1-x)$BaTiO_3$ composites; (b) Effective conductivity of the components assigned to the ceramic BT core, ceramic grain boundaries (GB) and to the Ag-BT interfaces as a function of Ag filling factor, as determined by impedance spectroscopy analysis by using a circuit with three parallel components *(Annex §6)*.

10^{-7} S/m (at 100 Hz) up to ≈5 × 10^{-6} S/m (at 1 MHz), and can be described by the universal dielectric response (Jonscher's law [35]):

$$\sigma_{ac}(f) = \sigma_{dc} + Af^n \quad (4)$$

where σ_{dc} is a frequency independent component (dc-conductivity) describing long-range charge transport, while the last term is usually assigned to localised hoping processes (A is a temperature-dependent pre-exponential term and n an integer number describing mechanisms of conduction and relaxation processes in different frequency ranges). The ultralow frequency-independent dc-conductivity plateau is not reached when reducing the frequency in these composites, although a tendency is somehow noticed for some compositions (*e.g.* 4, 5, 8–11, 15 vol.%), but only at high temperatures (≈180 °C), thus being due to thermally activated phenomena. This observation confirms the good dielectric character of all the investigated compositions. Moreover, at a given frequency, the conductivity takes quite similar values, without any dramatic increase in range, possible to be assigned to a dielectric-conductive transition. However, an indication about the tendency to approach the percolation limit (at least at local scale) is given by the slightly larger low frequency ac-conductivity values, which are placed in the range of: (10^{-6}, 5 × 10^{-6}) S/m for x = 5 and 20 vol.% and of (5 × 10^{-7}, 8 × 10^{-6}) S/m for x = 11.5 and 12 vol. % (values determined at 100 Hz).

The relaxations have been analysed by Arrhenius fits of the imaginary part of permittivity and of the dielectric modulus (*Annex, §5*). The corresponding activation energies (Fig. *S8, Annex*) have similar values as in BT ceramics, being mainly assigned to the contributions from the single and double ionised oxygen vacancies. Therefore, the presence of Ag filler does not dramatically alter the dielectric character derived from the BT matrix, which is preserved, irrespective of the metal filler level. No drop of the activation energy with orders in magnitude is observed for the compositions characterised by the highest permittivity levels, meaning that the good dielectric character is still maintained for all the investigated composites and the full percolation limit was not yet attained for any of the present compositions.

Further information concerning the composition dependence of the electrical properties was realised by Impedance Spectroscopy analysis (*Annex, §6*). The best fit of the complex impedance Nyquist plots $Z''(Z')$ in the frequency range (2 × 10^2, 10^6) MHz has been realized by assuming a model circuit containing a series of three parallel elements and one serial resistance R_s (Fig. *S9, Annex*). By this method [36–38] the contributions of different microstructural elements displaying over distinct frequency ranges can be deconvoluted: (i) bulk ceramic grains (R_{BT}, C_{BT}) which dominate the high frequency range and describe intrinsic transport and relaxation properties within the ceramic grain cores; (ii) ceramic grain boundaries (R_{GB}, CPE_{GB}) dominating the intermediate frequency range, where the resistive and capacitive characteristics are different than of the bulk due to the existence of compositional, structural and charged defects located at ceramic grain boundaries and (iii) metal-ceramic interfaces described by (R_{Ag-BT}, C_{Ag-BT}) elements, assigned to the Ag-BT boundaries within the CerMet volume and to the electrode-ceramic interfaces, which manifest predominantly at low frequencies and impact the charge transport. Although all the investigated composites are similar, the variation of porosity and of their geometrical parameters (size and plan-parallelism, the quality of electrode-ceramic interface) have an impact on the impedance responses. Therefore, the Impedance Spectroscopy analysis cannot give reference values for each circuit elements to be compared each other, but it can rather provide a guide concerning the range of their evolution *vs.* Ag filling factor. Such dependences of the model capacitances and resistances as a function of silver addition are shown in (Fig. *S11, Annex*). By assigning to each circuit component equivalent geometrical characteristics of the whole samples, an effective equivalent conductivity for each component was determined as a function of filling factor (Fig. 6, b). Interestingly, this picture indicates that close to some specific compositions, the effective equivalent conductivity assigned to the Ag-BT interfaces increase (almost two orders in magnitude at ≈4 and ≈20 vol.% and with less than one order in magnitude around 11.5–12 vol.%). Similarly, the effective conductivity corresponding to the ceramic grain boundaries also have maxima around the same compositions, with variations of around one order in magnitude. Since the conductivity does not skyrocket with 10^4–10^{10} orders in magnitude as in large-scale percolation cases [23], one may conclude that a permittivity increase is expected around the mentioned critical composition, as result of both the field enhancement between isolated non-conductive ceramic regions related to their specific microstructures, combined with short-range percolative-induced dielectric enhancement.

Due to the extrinsic relaxation contributions that overlap on the permittivity rise, it is important to compare the permittivity values as a function of composition at high frequency values. The percolation law [6,7] predicts a monotonic increase in permittivity towards gigantic values over the whole compositional range, for the same type of phase connectivity. Nonetheless, the collection of composites examined here exhibits an entirely distinct behaviour. Fig. 7 illustrates the composition dependence of permittivity (a) and tangent loss (b) determined at the frequency of 100 kHz, at 20 °C, in the range of O-T phase transformation, at 60 °C, in a full T state, and at the Curie temperature. The first observation is that all the samples preserve a very good dielectric character, with low dielectric losses between (1.5, 3.6)% for x ≤ 5 vol.% and even lower: in the range of (0.8, 2.2)% for higher Ag additions, as

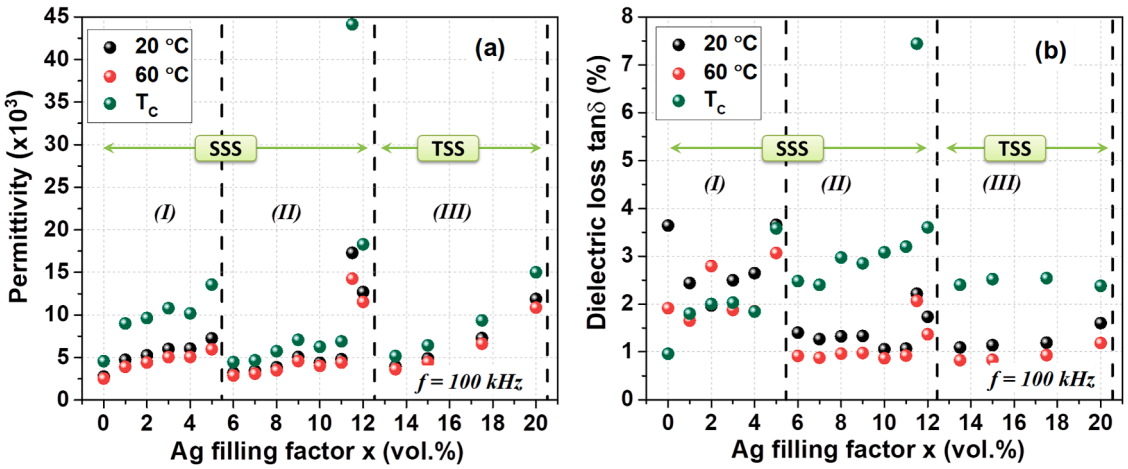


Fig. 7. Dependences on the Ag amount in the xAg-(1-x)$BaTiO_3$ CerMet composites of the: (a) permittivity and (b) tangent loss, at the temperatures of 20 °C (O-T transition range), 60 °C (T phase) and at the Curie temperature.

observed in Fig. 7, (b). Interestingly, the evolution of permittivity has not a monotonous increase with the Ag addition, but it presents three distinct regions denoted as *I, II* and *III* (Fig. 7, (a)). In each region the permittivity has a monotonous increase as a function of the filling factor and reaches a maximum around some critical compositions of about 5, 11.5 and ≥ 20 (vol.%), respectively, which were expected from the enhanced values of the capacitances corresponding to the ceramic grain, ceramic grain boundaries and to the metal-ceramic interfaces, observed in Fig. *S11, a, Annex*. Around the same critical compositional ranges, the dielectric losses are a bit higher (although still remaining good dielectrics), in agreement with the local minima of the equivalent resistances derived from the Impedance Spectroscopy analyses (Fig. *S11, b, Annex*).

The porosity always leads to a decrease in permittivity; however, it's important to note that the relationship between permittivity and composition in Fig. 7, (a) does not scale with the density changes illustrated in Fig. 2, (c). Nevertheless, the porosity variations should be taken into consideration when comparing the properties of the CerMet composites across the overall composition range, in particular for the samples with x > 12 sintered by TSS, for which the relative density reduced below 84%. To exclude this effect and focus solely on the role of metal addition in the dielectric response, effective field-based calculations [39] have been performed to estimate the dielectric constant corresponding to ideally fully densified samples. The corrected permittivity *vs.* the Ag composition shows the same trend, with three distinct regions, as presented in *Fig. S12, Annex*. This result led to the conclusion that for this set of composites, the permittivity rise in steps instead of a monotonous variation towards giant permittivity is determined by drastic microstructural modifications of the Ag inclusions at some given compositions. More specifically, the CerMets present partial percolation processes with permittivity enhancement close to the three critical concentrations around 5, 11.5, and ≥ 20 (vol.%), respectively. The fits of permittivity *vs.* composition *x* according to the percolation law [6,7] provided similar values for the parameters and for the critical concentrations, around the experimentally observed ones (*Table SII, Annex, §8*). For x ≤ 5 vol.% (region *I*), the permittivity rises about two times with respect to the $BaTiO_3$ value, and the increase is faster at low x additions than predicted by percolation laws [6,7] or by ones reported in other publications [19]. Similar results have been presented in ref [5]., in which the role of the processing parameters on the low and high field properties of $BaTiO_3$-based CerMet samples with low Ag additions have been investigated. Further, the permittivity reduces to a half between x = 5 and 6 (vol.%), as also observed in the corrected data in *Fig. S12, Annex*, and then increases with the silver addition in the region *II* and reaches the highest values around 11.5–12 vol.% (Fig. 7, (a)), which clearly is close to a threshold composition. The losses are a bit higher at this critical composition, but still below 2.5%, at 100 kHz. For the composites with higher x additions, for which the consolidation strategy was modified to TSS in order to conserve the nominal amount of Ag, all the samples with a lower relative density, in the range of 82–84% (Fig. 2, (c)) have a reduced permittivity. However, the room temperature permittivity decreases about three times between x = (12–13.5) vol.%, even when the role of porosity is discarded, according to the *Fig. S12, Annex*. It is worth to note that such a high permittivity is not specific to a single sample only: other prepared samples with the nominal composition of ≈11.5–12 (vol.%) show the same high level of permittivity increase, in the experimental error limits. This led to the conclusion that the concentration of ≈11.5–12 (vol.%) is placed indeed close to a threshold value for which a kind of partial percolation might take place at short range scale, due to specific microstructural factors accomplished around this composition. When increasing more the Ag addition in the compositional range *III*, a fast permittivity augmentation towards the total percolation expected at about ≥ 20 vol.% is again observed, in agreement with the predictions of the statistical percolation laws derived for equiaxed inclusions embedded in a continuous dielectric matrix, and also reported for the largest number of CerMet compounds [19–22 *and refs. herein*]. The same trend is observed at a room temperature of 20 °C in the range of O-T transition, at 60 °C in a full T state and at the Curie temperature, when higher permittivity values are reached, with the maximum value of ≈45,000 for x = 11.5 vol.% Ag, while preserving a good dielectric character (tanδ of ≈7.5%). It is important to note that the observed permittivity values did not really reach colossal values of ≈10^5–10^6 [22 *and refs herein*, 23]: at any temperature, the increase is less than one order in magnitude. Therefore, the present CerMets are still under-percolated at large-scale level, although some local percolations might occur as result of the formation of unusual Ag microstructures, which generate field intensification in some specific ceramic regions. Additionally, the overall low losses indicate the effective encapsulation of Ag inclusions inside the high resistance (of 10^7–10^8 Ω: *Fig. S11, b, Annex*) $BaTiO_3$ ceramic grains.

In order to gain a better knowledge concerning the particular microstructural features that provide enhanced permittivity values, the composites with x = 5, 11.5 and 20 (vol.%) with enhanced permittivity values have been selected to be thoroughly investigated using 3D methodologies combined with FEM simulations.

4.3. Tomographic microstructural investigations. numerical analysis of the correlation between the 3D microstructures and high permittivity values

The final CerMet microstructures (Ag size and shape, phase

interconnectivity, ceramic grain size, and densification) are determined through the combined processes of ceramic sintering and metal melting/infiltration/solidification during the high temperature treatment. Ag inclusions melt at 960 °C, migrate along the ceramic grains without wetting [40–42] due to the prominent volume expansion related to the oxygen uptake by the silver melt [43–45], and infiltrate through the open pores. When porosity is percolated, the melted metal moves at significant distances, join with other molten Ag zones, and form large elongated metallic regions embedded within the ceramic body, after the crystallization on cooling. On the other hand, if the pores are sealed off before the Ag melting process begins, the restriction of the metallic phase to small areas will primarily result in the production of equiaxed inclusions rather than elongated ones. When the Ag amount is small, the ceramic volume separating the Ag melts is sufficiently large, and the initial inclusions remain almost similar in size as in the starting powder mixture after the sintering, because they have fewer neighbors to join and form larger metallic structures [22].

As mentioned before, the composites sintered by SSS below 12 vol.% have a relative density in the range of (88, 91)% for $x \leq 4$ vol.% and rises to 94% for $x = 5$ vol.%. Consequently, it seems that the combination of an excellent densification and the development of elongated Ag zones, which cause a partial percolation of the ceramic regions in between, is what causes the permittivity rise in this composition. For $x = 5$ vol.%., the SEM-EDX analyses (Fig. 4, (a)) indicate both small and large equiaxed Ag aggregates unevenly distributed, together with a few longer structures. Increasing the amount of Ag upsurges the probability of forming percolated Ag channels inside the ceramic body. When using SSS method for compositions $x > 12$ vol.%, the samples are unable to retain all of the Ag amount within their volume, the melted metal increases its volume and escapes through the percolated pores, being drawn out towards the bulk composite surface. The critical compositions about 11–12 vol.% contain the highest Ag amount for which no significant Ag depletion took place, and the nominal composition could be preserved by the SSS procedure. Therefore, it results that the composition around (11.5 - 12) vol.% contains the largest amounts of elongated metallic inclusions in all the directions, and local percolated ceramic regions. It also has the highest density among all the CerMet series (r.d. of 95%) and these two cumulated factors explain its very high permittivity value, at a relatively low silver amount. Therefore, one can conclude that around the critical composition of ≈(11.5–12) vol.%, large scale displacement of melted Ag inside the percolated pores allowed the formation of elongated and tortuous Ag paths inside the ceramic volume, thus generated peculiar electric field distributions and high permittivity values. The micrograph of this composition shown in Fig. 4, (b) indeed indicates more elongated and curved microstructures.

For higher silver additions, the densification strategy had to be changed into a two-step sintering TSS process. The first heating step below the melting point of Ag, at 930 °C/12 h, allowed the pores to close and this prevented the melted Ag from migrating over great distances or being drawn out towards the sample interfaces during the second sintering step at higher temperature. The TSS strategy allowed the preservation of Ag composition on the expense of losing density (r.d. of 81.3–84% for $x \geq 13.5$ vol.%). The corresponding micrograph (Fig. 4, (c)) shows the formation of predominant small and large rounded aggregates of Ag, besides some elongated ones, and pores. For obtaining more valuable information concerning the Ag microstructures within the CerMet volume and for computing the local field inhomogeneity by using real 3D microstructures with the aim to understand their role on the resulted dielectric properties, 3D tomographic analyses have been further realized.

4.3.1. *XCT characterization and modeling of electric field distributions*

This part of the study was designed to decipher the specific microstructural details related to the experimentally obtained highest permittivity values. Therefore, three critical compositions have been selected for a detailed 3D tomographic examination: 5 vol.% (Ag-BT1), 11.5 vol.% (Ag-BT2) and 20 vol.% (AG-BT3). Micro X-ray computed tomography analysis (μ-XCT) [46] with a minimum focal spot size of 800 nm was employed, with the voxel size of 0.67 μm and the volume of interest (VOI) size of (615 × 520.6 × 45.6) μm^3. The obtained 3D μ-XCT data have been pre-processed by applying a median filter to enhance the image quality for the subsequent image analysis [47,48]. In the next step, a histogram-based global thresholding method was employed to segment the Ag regions from the $BaTiO_3$ matrix, on the basis of the gray values in the image data of each sample [47]. For simplification, the composites have been considered as di-phasic, *i.e.* the ceramic porosity was disregarded in a first approach. The specific morphology parameters were determined by using the skeletonization procedure [49] (to derive the mean inclusion diameters and their size distribution) and by determining the geometric tortuosity as the ratio between the geodesic (the shortest possible path) and the Euclidean distance (the shortest linear distance without any interfering structure) from surface to other points [50].

Fig. S13, Annex shows a 3D representation of the raw XCT data and of the determined Ag filler network for the three selected CerMet samples: Ag-BT1 (5 vol.%), Ag-BT2 (11.5 vol.%) and Ag-BT3 (20 vol.%), while Fig. 8 (a-c) presents the 3D representation of segmented volume of the binary data obtained by using the aforementioned processes, in which the silver network embedded into the $BaTiO_3$ ceramic matrix is shown in dark colour. The average equivalent Ag diameter is quite similar, of ≈5.1 μm (Ag-BT1), ≈3.1 μm (Ag-BT2) and slightly larger: of ≈6.8 μm for Ag-BT3. The metallic inclusion geometry is clearly different in the three cases. The segmentation accuracy was validated by computing the Ag volume fraction, which resulted as: ≈5.9, ≈11.9, and ≈20.2 (vol.%) for Ag-BT1, Ag-BT2 and Ag-BT3, respectively. By considering the approximations and the systems' complexity, these computed values correspond quite well with the expected nominal Ag amounts of each sample.

The skeletonization presented in Fig. 8 (d-f) reveals a few essential microstructural differences between the three compositions:

(i) The Ag clusters are the shortest in the sample Ag-BT1, with average size diameters of around 3–4 μm, as observed in Fig. 8, (d). This is related to the small metallic amount, which did not allow the large scale joining of Ag melts with ones from other regions. As a result, this composition contains predominantly equiaxed Ag inclusions, besides a few elongated structures;

(ii) In the Ag-BT2 vol (Fig. 8, (e)), long and very thin in diameter silver inclusions exhibiting tortuosity in all the sample's directions are predominant with an average value of 0.7–1.5 μm. This occurs because, with this composition, the metallic liquid phase traverses the open porosity during sintering, nearly percolating the overall dielectric sample by encountering similar structures. Therefore, long and thinner metallic filaments resulted after cooling. For slightly higher Ag additions, the melted metal fully percolates the sample and migrates out of it, so that the composition around 11.5–12 vol.% can be considered a critical percolation limit for this specific kind of 3D interconnected Ag filamentary structure, for which giant permittivity was indeed observed.

(iii) In the composition Ag-BT3, long and thicker in diameter (average values in the range of 3–5 μm) silver structures are observed (Fig. 8, (f)). Even though the Ag amount was higher, the applied consolidation strategy TSS allowed the closing of long-range porosity before the Ag melting. Thus, the metal mostly occupied the available sealed ceramic regions and formed thicker structures in the final sample, which is, unfortunately, characterised by a large porosity. As a consequence, this composition is still under-percolated, but is not far from the percolation limit. Its permittivity is enhanced by the presence of metallic inclusions, but not to giant values, because of the high porosity level.

Additional geometrical descriptors for the Ag filler microstructure

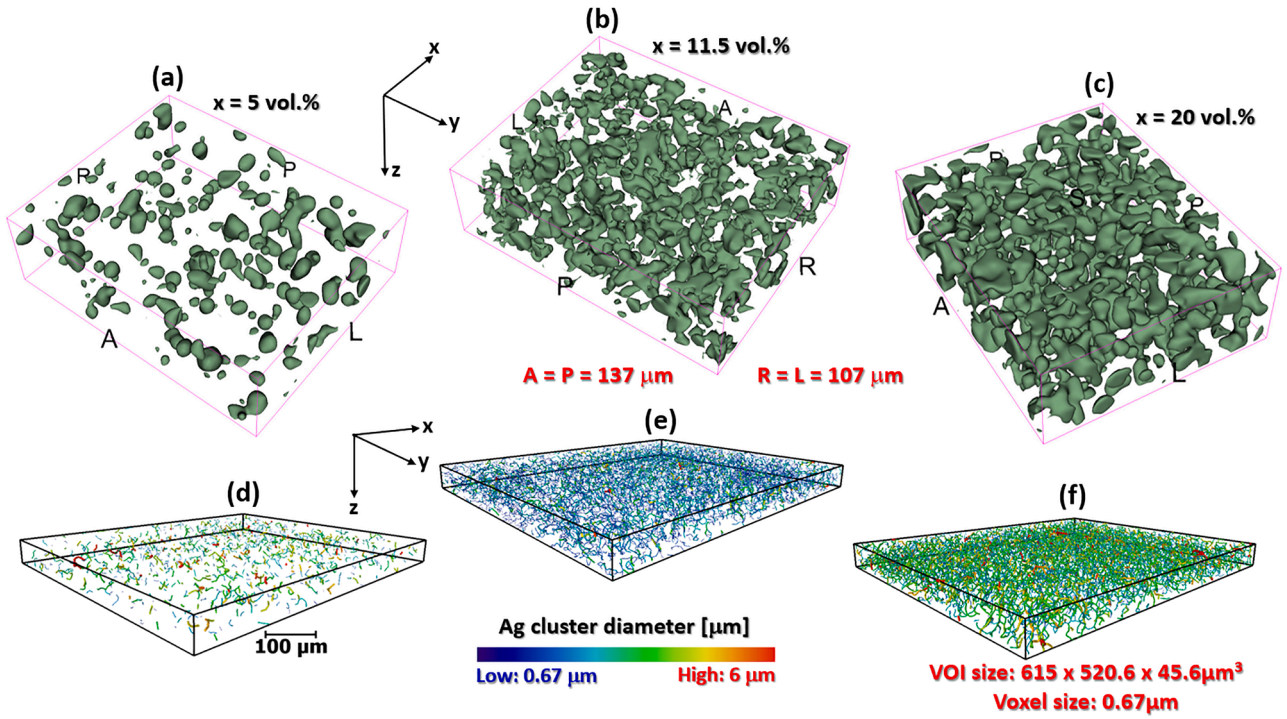


Fig. 8. Segmented 3D data for the CerMet samples Ag-BT1 (a), Ag-BT2 (b) and Ag-BT3 (c) indicating in dark colour the Ag inclusions for selected sample volumes; (d), (e), (f) Skeletonization of the three samples, in which the colour code gives information concerning the local diameter of the Ag inclusions (low – blue: 0.67 μm, high - red: 6 μm).

were extracted from the XCT-derived 3D volumes by using the same image-processing and statistical analysis methodology previously developed for porous electroceramics [29]. This analysis was comparatively realized for the samples with lower porosity only (AG-BT1 and Ag-BT2). After segmentation of the Ag phase, each voxel was assigned a binary variable V(x,y,z)=+1 for Ag and V(x,y,z)=−1 for the ceramic matrix. The spatial correlation functions $C_r(\Delta r)$ (r = x, y, z) were then calculated as directional autocorrelation functions of the voxel field, and the corresponding correlation lengths were estimated from the characteristic decay of these functions with distance. For the composition with 5 vol.% Ag, similar correlation lengths were obtained along the three axes ($\ell_x \approx 3.3$ μm, $\ell_y \approx 3.1$ μm, $\ell_z \approx 3.5$ μm), indicating a nearly isotropic Ag distribution at the investigated length scale. In contrast, for the composition with 11.5 vol.% Ag, larger correlation lengths were measured, particularly along the Oz direction ($\ell_x \approx 3.0$ μm, $\ell_y \approx 3.6$ μm, $\ell_z \approx 4.0$ μm), revealing an increased spatial continuity of the metallic phase consistent with the proximity to a critical percolation regime. In parallel, the Ag volume and interfacial surface area were determined from the segmented and slightly smoothed 3D reconstructions to ensure reliable surface estimation. Comparable specific surface-to-volume ratios were obtained for the two compositions (S/V ≈ 0.85 μm^{-1} for 5 vol.% Ag and S/V ≈ 0.82 μm^{-1} for 11.5 vol.% Ag), suggesting that the main microstructural difference between these compositions arises from changes in connectivity and correlation length rather than from a strong variation of the interfacial area density. The corresponding correlation functions and 3D surface renderings used for these calculations are provided in Figs. *S14, S15, Annex*.

Further, FEM calculations were conducted to compare the influence of the Ag filler microstructures on the local electric field distribution and their role in the permittivity enhancement. The analysis utilized 3D XCT-derived microstructures subjected to an electric field of 14 V/m applied on their plane-parallel horizontal surfaces.

Due to the fact that porosity also generates field distortions at the air-ceramic interfaces and to discuss mainly the role of the silver inclusions, the calculations have been performed on the dense composites only: Ag-BT1 (5 vol.%) and Ag-BT2 (11.5 vol.%). The resulting electric field maps are comparatively shown in Fig. 9(a) and (c), while the field distortions generated by the presence of Ag into the dielectric ceramic are observed in the 2D longitudinal and transversal sections in Fig. 9, (b) and (d), for the two compositions. As expected, due to the free charges screening, the Ag metallic inclusions are identified by the regions with zero field inside: dark regions in Fig. 9, (a) and (c) or white regions in the sections from Fig. 9, (b) and (d). The electric field is strongly inhomogeneous inside the sample volume and takes different values with respect to the external applied one, of 0.014 kV/m. Higher fields are encountering the metallic fillers and the highest values regions, which contribute to produce the largest permittivity, are concentrated in some small volumes in between the closer metallic inclusions (dark red in the scale colour). The highest fields can reach values above ≈10 times larger than the applied one. The field is also enhanced at the corners or sharp metallic regions in between the tortuous metallic elongated structures.

A better view concerning the field distribution inside the overall sample volume is observed in the normalized electric field histograms in the Fig. 9, (e) and (g), while the local contributions to the total permittivity are estimated from Eqs. (1) and (2) in Fig. 9, (f) and (h), where the local permittivity is proportional to the square of the normalized local field $\sim \left(E_{loc}/E_{appl}\right)^2$. The zero field regions are predominantly assigned to the metallic filler, but also to ceramic volumes confined inside metallic inclusions, which are fully screened from electrical point of view and do not contribute to the effective permittivity. Some other ceramic regions corresponding to near-zero or very low-field values give a small contribution to the effective permittivity because they are encountered by metallic clusters and they are partially screened. The largest sample's volume is subjected to fields higher than the external one, and these regions contribute to the effective permittivity with values slightly higher than those of the pure BT ceramic phase. The field distribution is larger and extended towards much higher field values for the composition of 11.5 vol.% with respect to 5 vol.% Ag. Consequently, a large number of regions subjected to very high fields will contribute producing a higher effective permittivity for this

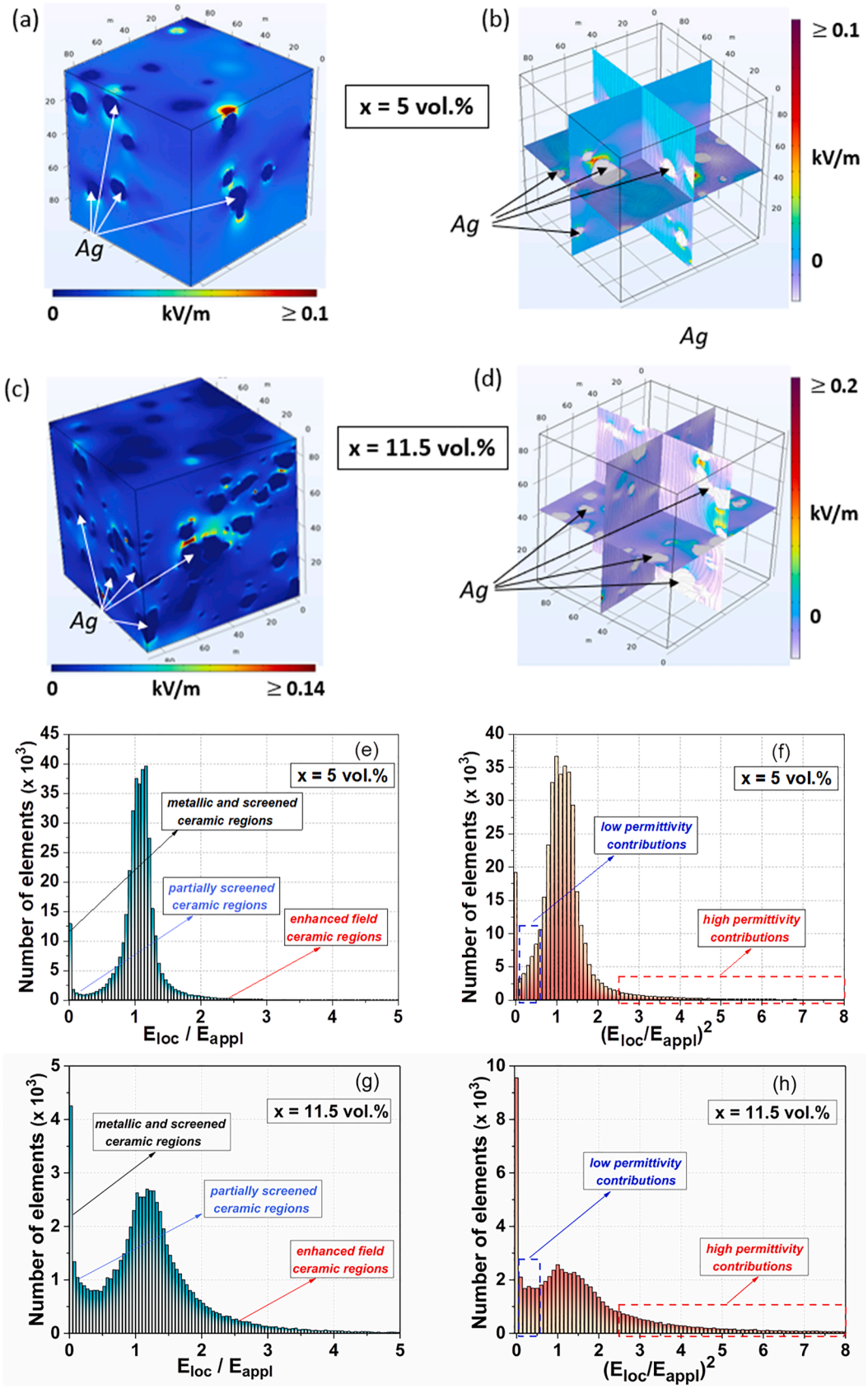


Fig. 9. (a), (c) 3D local field maps with transversal and longitudinal 2D sections (b), (d), with the corresponding field map scale resulted under the application of an electric field E_{appl} = 14 V/m; local field distributions (e), (g) and local permittivity distributions (f), (h) determined from the 3D XCT-derived microstructures for the dense CerMets: Ag-BT1 with x = 5 vol.% in (a), (b), (e), (f), and (b) Ag-BT2 with x = 11.5 vol.% in (c), (d), (g), (h). The electric field is normalized to the external applied value in the histograms.

composition, as experimentally was indeed observed.

4.3.2. SEM-FIB analyses and local field calculations

For a multi-scale view of the field distribution inside the Ag-BT composites and to achieve more specific microstructural details at improved resolution of the 3D microstructures at smaller scale, SEM-FIB analyses (slice & view) have been also performed (the SEM resolution being ≈10 nm, the area of a pixel is ≈5000 times smaller than a voxel face in the XCT analysis). As result, 2D sections within the samples were derived and then, FEM calculations were performed on such real microstructures in order to discuss their contribution to permittivity enhancement.

Fig. 10 presents a collection of a few images from the sample with a silver fraction of 11.5 vol.%, at an average distance of 3 μm apart. They have been selected in such a way to illustrate the microstructural complexity of these CerMet composites and to present in detail a few general characteristics of the microstructure, containing: (i) porous inclusions, comparable in size, which are evenly distributed; (ii) silver inclusions with twisted morphology, which tend to electrically shield some ceramic volumes, while leading to field accumulations in other different areas. For example, the two silver structures that can be observed in the first quadrant of the fifth section converge significantly towards the sixth section, where they neighbour what might be a single ceramic grain. They form a bridge after the sixth section, after which the entire metallic body shrinks in size; (iii) the expected behavior of a molten metal can be observed: as the metal cools down from the liquid phase, its volume tends to decrease, while due to adhesion forces, it tends to remain stuck to the inner walls of the ceramic channel it is occupying. From the equilibrium of this phenomena, hollow cones tend to form at the end of the channels, oftenly accompanied by cracks in the metallic volume. This kind of behavior is remarkable in the first four sections. From an electrical perspective, this can lead to very high field accumulations at the sharp points that are left behind by the volume decrease.

Irrespective of the investigated compositions, the following microstructural characteristics of Ag filler have been observed by 3D tomography in the investigated CerMet samples: (1) the Ag inclusions are inhomogeneous in sizes and shapes and form 3D tortuous complex networks; (2) the connectivity of the metal-ceramic phase is very complex and cannot be adequately represent by a simple (m, n) connectivity scheme [51]. It varies across different regions of the sample due to uncontrolled ceramic porosity closure and migration of melted Ag during the consolidation processes. Nevertheless, due to the small-scale migration and small metallic amounts, one can infer that the composites with low Ag quantities (x $\leq$ 5 vol.%) contain larger amounts of regions with $(0, 3)$ phase interconnectivity type metallic inclusions; (3) the Ag melts can partially or completely cover ceramic regions or pores; (4) fine inclusions in the range of the threshold limit of the XCT resolution are found in all the compositions. Given the fact that the resolution of the SEM lies in the region of 10 nm, the area of a single pixel is around 5000 times smaller than any voxel face present in the XCT. An example of such a structure is presented in Fig. 11, (a), in the form of a very thin silver connection, observable in the third quadrant of the FIB section; (5) the existence of some large Ag percolated aggregates even for low Ag additions; (6) the formation of Ag structures with necks, sharp corners or quasi-planar aspect in 2D sections, with a perfect contact with large faceted ceramic grains; (7) the formation of some longer and thinner tortuous structures with sharp ends, in particular for the composition with 11.5 vol.% Ag. Fig. 11 displays two sections through such structures where their sharp ends and twisted geometry can be observed. It is important to note that all the above-described types of Ag inclusions are present in all the compositions, but they are found in different amounts. In particular, x = 5 vol.% contains more $(0, 3)$ inclusions of different sizes along with elongated ones, while the highest permittivity composition x = 11.5 vol.% comprises the largest amount of thinnest elongated tortuous metallic structures. Such microstructure is close to the model ones proposed in the Fig. 1, *Configuration 2*, which predicted by FEM calculations the highest permittivity level at a percolation limit around 12 vol.%.

As an example, Fig. 11, (a) and (d) depict two selected 2D slices from the CerMet sample with the composition x = 11.5 vol.%, as resulted by SEM-FIB tomography. A few types of observed Ag filler inclusions inside the ceramic matrix, developed by the Ag melting/infiltration processes within the available porosity during sintering are observed: $(0, 3)$ - type equiaxed inclusions with rounded shape or with angular aspect and sharp corners either small or coarse, rounded inclusions fully covering a circular pore or neighboring a pore, elongated Ag inclusions with complex shapes partially covering ceramic regions extended over tens of μm in all the directions or elongated in one direction which may contain ultrathin necklines. By using such sections to compute the electric field by FEM in a 2D approximation, one may observe locally, the role of each such peculiar shape of metallic inclusion changes the local field at

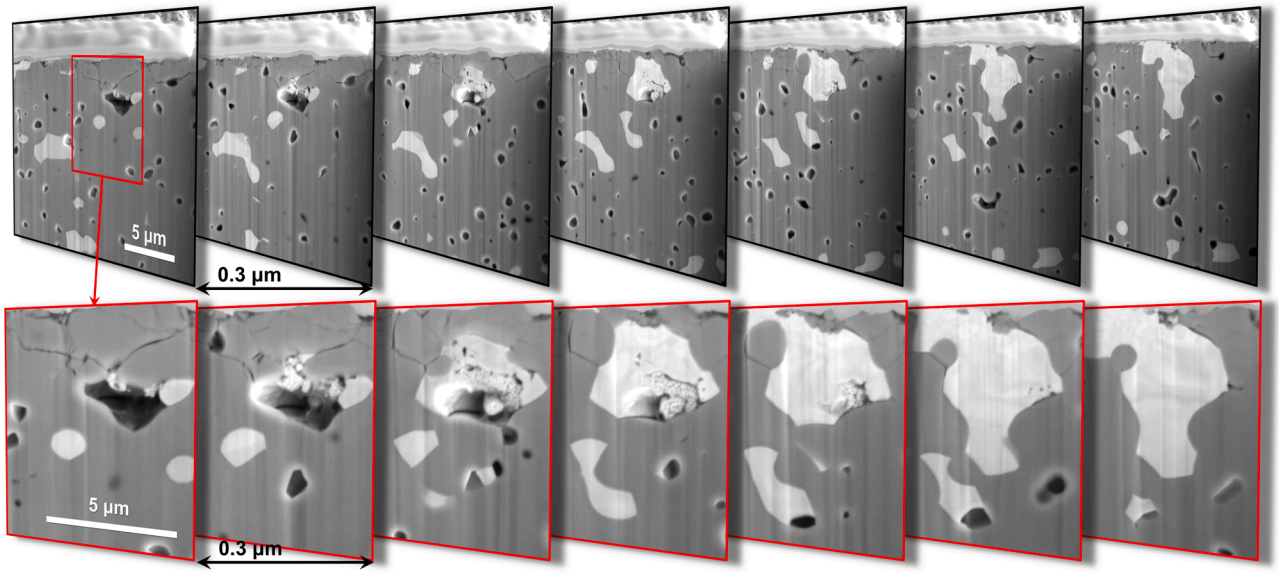


Fig. 10. Succession of seven 2D microstructures generated by SEM-FIB slice & view procedure in the ceramic sample with x = 11.5 vol.% showing details of the Ag microstructures evolution (composite overview – up and Ag structure detail – down) within the sample volume (white: Ag, dark: pores, grey: BT ceramic).

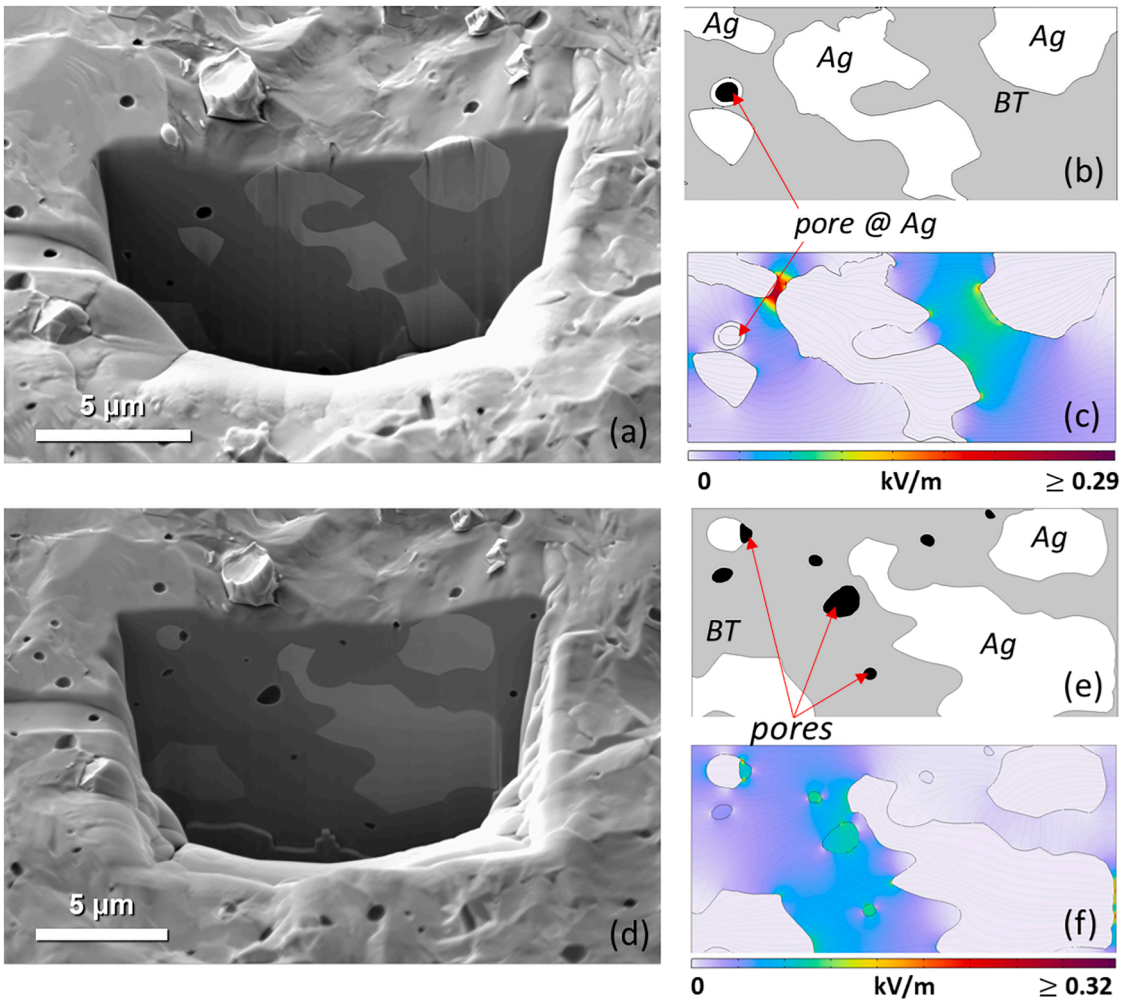


Fig. 11. SEM-FIB micrographs obtained in two different sample regions (a), (d); 2D model sections derived from the micrographs (b), (e) and the corresponding 2D - FEM field calculations performed in a 2D approach (e), (f), for the composition x = 11.5 vol.%. The field with an amplitude of 0.014 kV/m was applied horizontally on the lateral faces. The applied external field level is indicated by the red arrow in the color scale of the field maps (c) and (f).

micron-scale and try to assign them to the field and permittivity distributions presented in the Fig. 9, (g) and (h). The metallic regions, as well as the partially percolated ceramic areas contained inside a hollow region partially or completely closed by Ag shells are characterized by zero field (white regions in Fig. 11, (c), (f)). The dielectric regions inside cavities are partially screened, being subjected to very low fields; thus, they generate low permittivity contributions marked in Fig. 11, (f). The dense dielectric ceramic regions far from fillers or pores have a local field around the externally applied one, and they contribute with medium permittivity values corresponding to the maximum distributions in the Fig. 9, (e-h). The pores are field concentrators, *i.e.,* along the applied field direction (horizontal axis), the field is larger inside the pores than in the adjacent dielectric regions, if they are in a region not fully or partially screened by larger metallic fillers, like the "elephant"- shaped one in the right side of the Fig. 11, (d-f). However, the porosity regions do not generate permittivity increase, because the permittivity of the air pores is 1, about 10^3 lower than that of the ceramic regions. The metallic sharp ends are strong field concentrators, in particular if they are very close to other metallic inclusions (like the dark red regions in Fig. 11, (c)). Such areas correspond to the ultra-high field values and provide giant local permittivity responses. As Fig. 8 indicates, the composition with 11.5 vol.% Ag has an inherently different kind of inner geometry than the others that have been analysed. The result from the skeletonisation process (Fig. 8, (e)) suggests that, in this case, a thin, elongated, but twisted inclusion geometry is prevalent. This means that such silver structures may easily stretch over long distances, potentially covering a large amount of the distance between two opposing faces of the sample bulk, leaving very little room for ceramic interstices. Moreover, their elongated geometry can easily accommodate very sharp angles between the grain boundaries that surround them. This leads to high field build-ups, described empirically in Fig. 11, (c) and (f) and statistically in Fig. 9, (e) and (f), where the field accumulation peak tends to lean rightwards. It is proposed that such very localised but strong build-ups might be responsible for the very high overall permitivity values of this sample. Concerning the low additions of Ag, $x < 5$ vol.%, one may expect that mostly $(0,3)$ type of connectivity is formed, due to the fact that Ag melts do not find close neighbors to connect and the permittivity increase only as result of x increase, while the connectivity scheme remains almost the same. At the critical composition of ≈5 vol.%, most probably longer metallic structures with sharp ends started to form, and due to them, a first notable microstructural modification takes place around this composition. This fact provides regions of field increase and larger permittivity than expected by the predictions of percolation law for simple (0,3) connectivity scheme in usual CerMets [22].

Consequently, the 3D tomographic analyses provided important information concerning the overall CerMet microstructural details and revealed that even for the same sintering strategy (SSS), the microstructures (connectivity, size, and shape of the metallic filler) are not similar at any filler amount in all the investigated compositional range. This peculiar feature is related to the Ag melting, migration, joining, and

recrystallisation taking place at the same time with the grain joining, porosity closing, grain ceramic increasing and densification processes during the sample consolidation. The observed 3D microstructural details also explain that the largest permittivity enhancement is related to peculiar microstructures characterised by thin and long tortuous Ag filaments within the dense dielectric ceramic. No further FEM calculations for field and other electrical properties of the entire samples have been performed in the 3D approach due to the computational constraints of such very complex structures, to the statistical relevance of the selected volume for tomography analyses and to the resolution and segmentation limitations encountered in determining the 3D input microstructures. However, the local 3D microstructural analyses and the related 2D and 3D specific field calculations revealed the very important role of peculiar silver microstructures in determining multiple sub-percolative compositional ranges. They also explain the permittivity increase to remarkable high values in such composites, at lower filling volumes than the expected full percolation limit.

It is important to highlight that field concentration in certain sample volumes, while beneficial for enhancing permittivity, also invariably leads to a decrease in breakdown field. The CerMet breakdown field (though rarely reported) is always smaller than one corresponding to the bulk dielectric matrix (≈90–100 kV/cm for pure $BaTiO_3$ ceramics [9]), *e.g.* assumes values of 20–35 kV/cm or higher: ≈80 kV/cm, depending on the preparation method, filling factor and resulted microstructures [22 *and refs. herein*]. In this sense, a study containing FEM calculations for randomly dispersed metal inclusions into a dielectric matrix, completed with some experimental values [25], concluded that materials with colossal permittivity cannot be candidates for high capacitance applications, because the breakdown field decrease and permittivity increase are produced by the same mechanism of field enhancement generated by the boundary conditions at the metal-dielectric ceramic interfaces [25]. However, additionally to the field enhancement, other important factors related to the specific composition, samples' quality, structural and charged defects, geometrical parameters (*e.g.* phase connectivity scheme, core-shell structures, filler clustering) also play an essential role on the breakdown phenomena and have not been considered. All of these, together with adequate breakdown models should be employed in a reliable study, which is beyond the aim of the present work. Nevertheless, such a complex theoretical & experimental investigation concerning the crucial role of the microstructures on permittivity enhancement and breakdown field reduction may provide mitigation strategies by microstructural engineering to preserve the advantages of both electrical parameters, as discussed in the review [22].

5. Conclusions

The present study investigated the role of metallic microstructural changes on the intrinsic effective permittivity enhancement in composites formed by the addition of Ag metallic filler into a ferro-dielectric ceramic matrix of $BaTiO_3$. Field and permittivity calculations based on FEM for a few model systems revealed the critical role of the filler microstructures on the onset of percolation and on the permittivity variation upon the metal addition. Based on this observation, a set of xAg-(1-x)$BaTiO_3$ CerMet composites with compositions in the range of $0 \leq x \leq 20$ vol.% have been prepared and investigated in detail from a dielectric point of view. The concentration dependence of the dielectric properties revealed compositional ranges for which the permittivity increases according to the percolation law, which are limited by some critical compositions around the values of 5 vol.% and 11.5 vol.%, where drastic microstructures and connectivity scheme alterations take place. These microstructural changes result from Ag melting during the sintering, which allows it to migrate and join with other melted regions in any direction to form longer tortuous metallic inclusions inside the ceramic matrix. In particular, based on the observed microstructural features and FEM field and permittivity calculations based on the tomography-derived 3D microstructures, the thinner and elongated filler inclusions provided the highest permittivity increase. Further studies are necessary to understand to what extent it is possible to control the favourable microstructures by specific ceramic processing and how it is possible to reduce the breakdown failure in the regions subjected to the highest fields. It is worth noting that only intrinsic dielectric contributions generated by the field inhomogeneity have been analysed here. However, the composition 11.5 vol.% is also rich in relaxations with respect to the other compositions, mostly at low frequencies. The relaxations are related to the presence of a large number of metal-dielectric interfaces where uncompensated screened charges are located. These slow species (mostly oxygen vacancies simple and double ionised) move under the alternative fields and extrinsically contribute to the final values of permittivity. The role of microstructures in these relaxations and their involvement in the permittivity increase is worth to investigating in detail in a dedicated study. In the particular case when the metallic filler undergoes melting during the sintering process, the connectivity scheme is not maintained throughout the entire compositional range, even when using the same sintering parameters. Multiple percolation and permittivity increase occur at few threshold compositions, each one being characterized by a peculiar microstructure. The observed features explain the wide variability of permittivity *vs.* Ag addition trends reported in the literature [22 *and refs. herein*].

CRediT authorship contribution statement

Ina Turcan: Investigation, Formal analysis, Data curation. **Leontin Padurariu:** Validation, Software, Methodology. **Vlad Alexandru Lukacs:** Writing – original draft, Investigation, Formal analysis, Data curation. **Radu Stefan Stirbu:** Visualization, Software, Methodology. **Cristina Elena Ciomaga:** Investigation, Formal analysis, Data curation. **Roxana Elena Patru:** Formal analysis, Investigation. **Fereshteh Falah Chamasemani:** Visualization, Software. **Roland Brunner:** Software, Formal analysis. **George Stoian:** Validation, Investigation. **Liliana Mitoseriu:** Writing – review & editing, Writing – original draft, Supervision, Funding acquisition, Conceptualization. **Donatella Giuranno:** Validation, Supervision, Resources, Conceptualization.

Declaration of competing interest

The authors declare that they have no known competing financial interests or personal relationships that could have appeared to influence the work reported in this paper.

Acknowledgements

This work was supported by the Romanian UEFISCDI PN-IV-P1-PCE-2023–0995 project (CERMETCOM); 3D slice & view SEM-FIB experiments were realised at Fraunhofer IPMS under the project ASCENT+ Access to European Infrastructure for Nanoelectronics (EU Horizon 2020 Programme Grant No 871130). The authors acknowledge dr. Lavinia Curecheriu (Alexandru Ioan Cuza University of Iasi) for support in the sample preparation.

Supplementary materials

Supplementary material associated with this article can be found, in the online version, at doi:10.1016/j.actamat.2026.122638.

References

[1] J.S. Moya, S. Lopez-Esteban, C. Pecharroman, The challenge of ceramic/metal microcomposites and nanocomposites, Prog. Mater. Sci. 52 (2007) 1017–1090, https://doi.org/10.1016/j.pmatsci.2006.09.003.

[2] L. Bolzoni, Structural electroactive cermets: dielectric and structural properties of conductive metallic reinforced piezoelectric ceramics, Crit. Rev. Solid State Mater. Sci. 46 (2021) 38–81, https://doi.org/10.1080/10408436.2019.1690422.

[3] S.A. Jose, M. John, P.L. Menezes, Cermet systems: synthesis, properties, and applications, Ceramics 5 (2022) 210–236, https://doi.org/10.3390/ceramics5020018.

[4] L. Padurariu, Numerical Models for Describing Dielectric & Ferroelectric Properties in Composites Systems, PhD Thesis, Univ. Al.I. Cuza Iasi, Romania, 2014.

[5] I. Turcan, V.A. Lukacs, L. Curecheriu, L. Padurariu, C.E. Ciomaga, M. Airimioaei, G. Stoian, N. Lupu, L. Mitoseriu, Microstructure and dielectric properties of Ag-$BaTiO_3$ composite ceramics, J. Eur. Ceram. Soc. 38 (2018) 5420–5429, https://doi.org/10.1016/j.jeurceramsoc.2018.08.002.

[6] M. Sahini, M. Sahimi, Applications of Percolation Theory, CRC Press, 1994, https://doi.org/10.1201/9781482272444.

[7] C.W. Nan, Y. Shen, J. Ma, Physical properties of composites near percolation, Annu. Rev. Mater. Res. 40 (2010) 131–151, https://doi.org/10.1146/annurev-matsci-070909-104529.

[8] V.A. Lukacs, I. Turcan, L. Padurariu, L. Curecheriu, A. Cernescu, G. Stoian, C. E. Ciomaga, F. Tufescu, N. Lupu, L. Mitoseriu, Nonlinear dielectric properties of $BaTiO_3$ - silver composites: the role of microstructure, J. Alloys Compds. 817 (2020) 153336, https://doi.org/10.1016/j.jallcom.2019.153336.

[9] (a) S. Panteny, C.R. Bowen, R. Stevens, Characterisation of barium titanate-silver composites, part I: microstructure and mechanical properties, J. Mater. Sci. 41, 3837–3843 (2006); https://doi.org/10.1007/s10853-005-5163-x; (b) S. Panteny, C.R. Bowen, R. Stevens, Characterisation of barium titanate-silver composites part II: electrical properties, J. Mater. Sci. 41, 3845–3851 (2006); https://doi.org/10.1007/s10853-005-5162-y.

[10] (a) C.Y. Chen, W.H. Tuan, Evaporation of silver during cofiring with barium titanate, J. Am. Ceram. Soc. 83, 1693–1698 (2000); https://doi.org/10.1111/j.1151-2916.2000.tb01451.x; (b) C.Y. Chen, W.H. Tuan, Effect of silver on the sintering and grain-growth behavior of barium titanate, J. Am. Ceram. Soc. 83, 2988–2992 (2000); https://doi.org/10.1111/j.1151-2916.2000.tb01671.x.

[11] F. Du, P. Yu, B. Cui, H. Cheng, Z. Chang, Preparation and characterization of monodisperse Ag nanoparticles doped barium titanate ceramics, J. Alloys Compds. 478 (2009) 620–623, https://doi.org/10.1016/j.jallcom.2008.11.099.

[12] P. Yu, B. Cui, Z. Chang, Preparation and characterization of Ag-doped $BaTiO_3$ based X7R ceramics, Mater. Res. Bull. 44 (2009) 893–897, https://doi.org/10.1016/j.materresbull.2008.08.015.

[13] P. Ren, H. Fan, X. Wang, J. Shi, Effects of silver addition on microstructure and electrical properties of barium titanate ceramics, J. Alloys Compds. 509 (2011) 6423–6426, https://doi.org/10.1016/j.jallcom.2011.03.077.

[14] Z. Wang, P. Xie, G. Fan, Z. Zhang, Y. Liu, Q. Guc, R. Fan, Epsilon-negative behavior of $BaTiO_3$/Ag metacomposites prepared by an *in situ* synthesis, Ceram. Intern. 46 (2020) 9342–9346, https://doi.org/10.1016/j.ceramint.2019.12.191.

[15] E.H. Baker, J.K. Johnstone, Effect of oxygen pressure on the melting of silver, Nature 205 (1965) 65–66, https://doi.org/10.1038/205065a0.

[16] X. Bao, M. Muhler, Th. Schedel-Niedrig, R. Schlogl, Interaction of oxygen with silver at high temperature and atmospheric pressure: a spectroscopic and structural analysis of a strongly bound surface species, Phys. Rev. B. 54 (1996) 2249–2262, https://doi.org/10.1103/PhysRevB.54.2249.

[17] A.J. Nagy, G. Mestl, D. Herein, G. Weinberg, E. Kitzelmann, R. Schlogl, The correlation of subsurface oxygen diffusion with variations of silver morphology in the silver–Oxygen system, J. Catal. 182 (1999) 417–429, https://doi.org/10.1006/jcat.1998.2388.

[18] S. Panteny, C.R. Bowen, R. Stevens, Characterisation of barium titanate-silver composites part II: electrical properties, J. Mater. Sci. 41 (2006) 3845–3851. https://link.springer.com/article/10.1007/s10853-005-5162-y.

[19] Y.J. Li, M. Xu, J.Q. Feng, Z.M. Dang, Dielectric behavior of a metal-polymer composite with low percolation threshold, Appl. Phys. Lett. 89 (2006) 072902, https://doi.org/10.1063/1.2337157.

[20] D.W. Kim, J.H. Lim, J. Yu, Efficient prediction of the electrical conductivity and percolation threshold of nanocomposite containing spherical particles with three-dimensional random representative volume elements by random filler removal, Compos. B. 168 (2019) 387–397, https://doi.org/10.1016/j.compositesb.2019.03.038.

[21] M. Khodaei, M. Jafaraghaei, A. Ajrian, S. Giahkar, Review of the percolation threshold for spherocylinder-based systems in a continuum model, Phys. A. 680 (2025) 131044, https://doi.org/10.1016/j.physa.2025.131044.

[22] L. Mitoseriu, V.A. Lukacs, L. Padurariu, C.E. Ciomaga, F. Gheorghiu, N. Horchidan, D. Giuranno, Emergent electrical properties in metal-ceramic composites: a critical revue, Ceram. Int. 51 (2025) 43459–43487, https://doi.org/10.1016/j.ceramint.2025.07.137.

[23] H. Du, X. Lin, H. Zheng, B. Qu, Y. Huang, D. Chu, Colossal permittivity in percolative ceramic/metal dielectric composites, J. Alloys Compds. 663 (2016) 848–861, https://doi.org/10.1016/j.jallcom.2015.12.171.

[24] C. Padurariu, L. Padurariu, L. Curecheriu, C. Ciomaga, N. Horchidan, C. Galassi, L. Mitoseriu, Role of the pore interconnectivity on the dielectric, switching and tunability properties of PZTN ceramics, Ceram. Int. 43 (2017) 5767–5773, https://doi.org/10.1016/j.ceramint.2017.01.123.

[25] J.I. Roscow, C.R. Bowen, D.P. Almond, Breakdown in case for materials with giant permittivity? ACS. Energy Lett. 2 (2017) 2264–2269, https://doi.org/10.1021/acsenergylett.7b00798.

[26] L. Mitoseriu, L.P. Curecheriu, Nanostructured Barium titanate ceramics: intrinsic *versus* extrinsic size effects, in: M. Alguero, J.M. Gregg, L. Mitoseriu (Eds.), Nanoscale Ferroelectrics and Multiferroics: Key Processing and Characterization Issues, and Nanoscale Effects, Wiley, 2016, pp. 473–501, https://doi.org/10.1002/9781118935743.ch15, eds.)Ch. 15.

[27] V. Buscaglia, C.A. Randall, Size and scaling effects in barium titanate. An overview, J. Eur. Ceram. Soc. 40 (2020) 3744–3758, https://doi.org/10.1016/j.jeurceramsoc.2020.01.021.

[28] A.C. Larson, R.B. Von Dreele, General structure analysis system, Los Alamos national laboratory, LAUR. ftp://ftp.lanl.gov/public/gsas, 2000.

[29] R.S. Stirbu, L. Padurariu, F.F. Chamasemani, R. Brunner, L. Mitoseriu, Mesoscale models for describing the formation of anisotropic porosity and strain-stress distributions during the pressing step in electroceramics, Mater. (Basel) 15 (2022) 6839, https://doi.org/10.3390/ma15196839.

[30] L. Padurariu, F.F. Chamasemani, R. Brunner, L.P. Curecheriu, V.A. Lukacs, R. S. Stirbu, C.E. Ciomaga, L. Mitoseriu, Analysis of local *vs.* macroscopic properties of porous $BaTiO_3$ ceramics based on 3D reconstructed ceramic microstructures, Acta Mater. 255 (2023) 119084, https://doi.org/10.1016/j.actamat.2023.119084.

[31] S.J. Shih, W.H. Tuan, Solubility of silver and palladium in $BaTiO_3$, J. Am. Ceram. Soc. 87 (2004) 401–407, https://doi.org/10.1111/j.1551-2916.2004.00401.x.

[32] V. Buscaglia, M.T. Buscaglia, G. Canu, $BaTiO_3$-based ceramics: fundamentals, properties and applications, Encycl. Mater.: Tech. Ceram. Glas. 3 (2021) 311–344, https://doi.org/10.1016/B978-0-12-803581-8.12132-0.

[33] M. Zheng, C. Zhao, X. Yan, R. Khachaturyan, F. Zhuo, Y. Hou, J. Koruza, Metal particle composite hardening in Ba0.85Ca0.15Ti0.90Zr0.10O3 piezoceramics, Adv. Funct. Mater. 33 (2023) 2301356, https://doi.org/10.1002/adfm.202301356.

[34] B. Darinskii, A. Sidorkin, A. Sigov, N. Popravko, Influence of depolarizing fields and screening effects on phase transitions in ferroelectric composites, Mater. (Basel) 11 (2018) 85, https://doi.org/10.3390/ma11010085.

[35] A.K. Jonscher, Dielectric Relaxation in Solids, Chelsea Dielectrics Press, London, UK, 1983.

[36] J.T.S. Irvine, D.C. Sinclair, A.R. West, Electroceramics: characterization by impedance spectroscopy, Adv. Mater. 2 (1990) 132–138, https://doi.org/10.1002/adma.19900020304.

[37] R. Holze, Impedance spectroscopy, J. Solid State Electrochem. 12 (2008) 651–653, https://doi.org/10.1007/s10008-007-0260-1.

[38] S. Pandey, D. Kumar, O. Parkash, L. Pandey, Equivalent circuit models using CPE for impedance spectroscopy of electronic ceramics, Integr. Ferroel. 183 (2017) 141–162, https://doi.org/10.1080/10584587.2017.1376984.

[39] L. Curecheriu, V.A. Lukacs, L. Padurariu, G. Stoian, C.E. Ciomaga, Effect of porosity on functional properties of lead-free piezoelectric $BaZr_{0.15}Ti_{0.85}O_3$ porous ceramics, Mater. (Basel) 13 (1–10) (2020) 3324. https://www.mdpi.com/1996-1944/13/15/3324.

[40] T. Sydorenko, Y.V. Naidich, Wettability by liquid metals, metalization, and brazing of Barium titanate ceramics a study investigates the contact interaction and wetting of $BaTiO_3$ perovskite ceramics by liquid metals, Weld. Journ. 93 (2014) 6S–14S. https://s3.amazonaws.com/WJ-www.aws.org/supplement/WJ_2014_01_s6.pdf.

[41] C.Y. Lee, M. Dupeux, W.H. Tuan, Adhesion strength of Ag/$BaTiO_3$ interface, Scr. Mater. 54 (2006) 453–457, https://doi.org/10.1016/j.scriptamat.2005.10.020.

[42] G. Canu, F. Valenza, Effect of Zr content on the wetting of $BaTi_{1-x}Zr_xO_3$ perovskite ceramics by Ag-based liquids, J. Eur. Ceram. Soc. 42 (2022) 3886–3891, https://doi.org/10.1016/j.jeurceramsoc.2022.03.040.

[43] E.H. Baker, J.K. Johnstone, Effect of oxygen pressure on the melting of silver, Nature 205 (1965) 65–66, https://doi.org/10.1038/205065a0.

[44] X. Bao, M. Muhler, Th. Schedel-Niedrig, R. Schlogl, Interaction of oxygen with silver at high temperature and atmospheric pressure: a spectroscopic and structural analysis of a strongly bound surface species, Phys. Rev. B. 54 (1996) 2249–2262, https://doi.org/10.1103/PhysRevB.54.2249.

[45] A.J. Nagy, G. Mestl, D. Herein, G. Weinberg, E. Kitzelmann, R. Schlogl, The correlation of subsurface oxygen diffusion with variations of silver morphology in the silver–Oxygen system, J. Catal. 182 (1999) 417–429, https://doi.org/10.1006/jcat.1998.2388.

[46] R. Hanke, T. Fuch, M. Salamon, S. Zabler, X-ray microtomography for materials characterization. Materials Characterization Using Nondestructive Evaluation (NDE) Methods, 2016, pp. 45–79, https://doi.org/10.1016/B978-0-08-100040-3.00003-1.

[47] T. Vorauer, P. Kumar, C.L. Berhaut, F.F. Chamasemani, P.H. Jouneau, D. Aradilla, S. Tardif, S. Pouget, B. Fuchsbichler, L. Helfen, S. Atalay, W.D. Widanage, S. Koller, S. Lyonnard, R. Brunner, Multi-scale quantification and modeling of aged nanostructured silicon-based composite anodes, Commun. Chem. 3 (2020) 1–11, https://doi.org/10.1038/s42004-020-00386-x, 202031.

[48] L. Padurariu, F.F. Chamasemani, R. Brunner, L.P. Curecheriu, V.A. Lukacs, R. S. Stirbu, C.E. Ciomaga, L. Mitoseriu, Analysis of local *vs.* macroscopic properties of porous $BaTiO_3$ ceramics based on 3D reconstructed ceramic microstructures, Acta Mater. 255 (2023) 119084, https://doi.org/10.1016/j.actamat.2023.119084.

[49] P. Iassonov, T. Gebrenegus, M. Tuller, Segmentation of X-ray computed tomography images of porous materials: a crucial step for characterization and quantitative analysis of pore structures, Water Resour. Res. 45 (2009) W09415, https://doi.org/10.1029/2009WR008087.

[50] A. Wijaya, B. Eichinger, F.F. Chamasemani, B. Sartory, R. Hammer, V. Maier-Kiener, D. Kiener, M. Mischitz, R. Brunner, Multi-method characterization approach to facilitate a strategy to design mechanical and electrical properties of sintered copper, Mater. Des. 197 (2021) 109188, https://doi.org/10.1016/j.matdes.2020.109188.

[51] R.E. Newnham, D.P. Skinner, L.E. Cross, Connectivity and piezoelectric-pyroelectric composites, Mater. Res. Bull. 13 (1978) 525–536, https://doi.org/10.1016/0025-5408(78)90161-7.